The Astrophysical Journal, 791:81 (21pp), 2014 August 20 doi:10.1088/0004-637X/791/2/81

THE 2–79 keV X-RAY SPECTRUM OF THE CIRCINUS GALAXY WITH *NuSTAR*, *XMM-Newton*, AND *CHANDRA*: A FULLY COMPTON-THICK ACTIVE GALACTIC NUCLEUS

P. Arévalo[1,2], F. E. Bauer[1,3,4], S. Puccetti[5,6], D. J. Walton[7], M. Koss[8], S. E. Boggs[9], W. N. Brandt[10,11], M. Brightman[12], F. E. Christensen[13], A. Comastri[14], W. W. Craig[9,15], F. Fuerst[7], P. Gandhi[16], B. W. Grefenstette[7], C. J. Hailey[17], F. A. Harrison[7], B. Luo[10,11], G. Madejski[18], K. K. Madsen[7], A. Marinucci[19], G. Matt[19], C. Saez[1,20], D. Stern[21], M. Stuhlinger[22], E. Treister[23], C. M. Urry[24], and W. W. Zhang[25]

[1] Instituto de Astrofísica, Facultad de Física, Pontificia Universidad Católica de Chile, 306, Santiago 22, Chile
[2] Instituto de Física y Astronomía, Facultad de Ciencias, Universidad de Valparaíso, Gran Bretana No. 1111, Playa Ancha, Valparaíso, Chile
[3] Millennium Institute of Astrophysics
[4] Space Science Institute, 4750 Walnut Street, Suite 205, Boulder, CO 80301, USA
[5] ASDC-ASI, Via del Politecnico, I-00133 Roma, Italy
[6] INAF Osservatorio Astronomico di Roma, via Frascati 33, I-00040 Monte Porzio Catone (RM), Italy
[7] Cahill Center for Astronomy and Astrophysics, California Institute of Technology, Pasadena, CA 91125, USA
[8] Institute for Astronomy, Department of Physics, ETH Zurich, Wolfgang-Pauli-Strasse 27, CH-8093 Zurich, Switzerland
[9] Space Sciences Laboratory, University of California, Berkeley, CA 94720, USA
[10] Department of Astronomy and Astrophysics, The Pennsylvania State University, University Park, PA 16802, USA
[11] Institute for Gravitation and the Cosmos, The Pennsylvania State University, University Park, PA 16802, USA
[12] Max-Planck-Institut für extraterrestrische Physik, Giessenbachstrasse 1, D-85748, Garching bei München, Germany
[13] Danish Technical University, Lyngby, Denmark
[14] INAF–Osservatorio Astronomico di Bologna, Via Ranzani 1, I-40127 Bologna, Italy
[15] Lawrence Livermore National Laboratory, Livermore, CA 94550, USA
[16] Department of Physics, Durham University, South Road, Durham, DH1 3LE, UK
[17] Columbia Astrophysics Laboratory and Department of Physics, Columbia University, 550 West 120th Street, New York, NY 10027, USA
[18] Kavli Institute for Particle Astrophysics and Cosmology, SLAC National Accelerator Laboratory, Stanford University, 2575 Sand Hill Road M/S 29, Menlo Park, CA 94025, USA
[19] Dipartimento di Matematica e Fisica, Università degli Studi Roma Tre, via della Vasca Navale 84, I-00146 Roma, Italy
[20] Department of Astronomy, University of Maryland, College Park, MD 20742-2421, USA
[21] Jet Propulsion Laboratory, California Institute of Technology, Pasadena, CA 91109, USA
[22] European Space Astronomy Centre (ESAC), ESA, P.O. Box 78, E-28691 Villanueva de la Cañada, Madrid, Spain
[23] Universidad de Concepción, Departamento de Astronomía, Casilla 160-C, Concepción, Chile
[24] Yale Center for Astronomy and Astrophysics, Physics Department, Yale University, P.O. Box 208120, New Haven, CT 06520-8120, USA
[25] NASA Goddard Space Flight Center, Greenbelt, MD 20771, USA
Received 2013 December 23; accepted 2014 June 11; published 2014 July 30

ABSTRACT

The Circinus galaxy is one of the closest obscured active galactic nuclei (AGNs), making it an ideal target for detailed study. Combining archival *Chandra* and *XMM-Newton* data with new *NuSTAR* observations, we model the 2–79 keV spectrum to constrain the primary AGN continuum and to derive physical parameters for the obscuring material. *Chandra*'s high angular resolution allows a separation of nuclear and off-nuclear galactic emission. In the off-nuclear diffuse emission, we find signatures of strong cold reflection, including high equivalent-width neutral Fe lines. This Compton-scattered off-nuclear emission amounts to 18% of the nuclear flux in the Fe line region, but becomes comparable to the nuclear emission above 30 keV. The new analysis no longer supports a prominent transmitted AGN component in the observed band. We find that the nuclear spectrum is consistent with Compton scattering by an optically thick torus, where the intrinsic spectrum is a power law of photon index $\Gamma = 2.2$–2.4, the torus has an equatorial column density of $N_{\rm H} = (6\text{–}10) \times 10^{24}$ cm^{-2}, and the intrinsic AGN 2–10 keV luminosity is $(2.3\text{–}5.1) \times 10^{42}$ erg s^{-1}. These values place Circinus along the same relations as unobscured AGNs in accretion rate versus Γ and L_X versus $L_{\rm IR}$ phase space. *NuSTAR*'s high sensitivity and low background allow us to study the short timescale variability of Circinus at X-ray energies above 10 keV for the first time. The lack of detected variability favors a Compton-thick absorber, in line with the spectral fitting results.

Key words: galaxies: active – galaxies: individual (Circinus) – galaxies: Seyfert – X-rays: galaxies

Online-only material: color figures

1. INTRODUCTION

The Circinus galaxy, hereafter referred to as Circinus, at a distance of ∼4.2 Mpc (Freeman et al. 1977), contains one of the closest active galactic nuclei (AGNs), and shows signatures of both starburst activity and black hole accretion. The presence of an AGN was initially inferred from high-ionization lines observed in the optical and IR bands. Moorwood & Glass (1984) classified the galaxy as a Seyfert 2 based on the high [N II]/Hα ratio and narrow emission lines. This identification was confirmed by the energy input required to produce the observed highly ionized coronal lines (Oliva et al. 1994). The Seyfert nucleus is obscured from direct view, but the broad line region is visible in reflection, through polarized light (Oliva et al. 1998).

Greenhill et al. (2003) detected H_2O maser emission consistent with a warped edge-on disk as close in as 0.1 pc from the nucleus. With a line-of-sight velocity of the innermost disk of 260 km s^{-1}, this observation implies a black hole mass of $1.5 \times 10^6\ M_\odot$, consistent with the dynamical upper limit of $4 \times 10^6\ M_\odot$ obtained by Maiolino et al. (1998). The bolometric luminosity, $L_{\rm bol} = 4 \times 10^{43}$ erg s^{-1}, has been estimated from the mid-IR nuclear spectrum, which is identified as reprocessed

AGN emission (Moorwood et al. 1996). Combined with the black hole mass estimate, this luminosity equals 20% of the Eddington luminosity. Therefore, Circinus contains a Seyfert nucleus, similar in mass and accretion rate to other well known local Seyferts, in particular NGC 4051 (Peterson et al. 2004; Woo & Urry 2002), but which is highly obscured from our line of sight. The obscuring material does not cover the entire central engine, as evidenced by the prominent ionization cone observable in [O III] line emission (Marconi et al. 1994).

Circinus was identified as an X-ray source for the first time by Brinkmann et al. (1994) using data from the *ROSAT* All Sky Survey. Matt et al. (1996) discovered strong Fe Kα emission with an equivalent width of 2 keV and a hard continuum from a pointed *ASCA* observation. This observation revealed strong Compton reflection in this source, produced by an AGN heavily obscured by cold circumnuclear matter, consistent with the Seyfert 2 nature of its optical spectrum. Matt et al. (1999) and Guainazzi et al. (1999) also found an excess of X-ray emission at higher energies using the *BeppoSAX* PDS instrument, interpreted as Compton-scattered and transmitted AGN continuum through clouds of high column density, identified with the molecular torus. The Compton shoulder of the Fe lines proves that the cold reflection is produced by Compton thick matter, supporting a scenario where the scatterer and obscurer are the same structure (Bianchi et al. 2002; Molendi et al. 2003). The width of the neutral Fe lines supports the interpretation of the torus, or other structures further out, as the optically thick reflecting material. Shu et al. (2011) measured a FWHM of 1710 km s^{-1} for the Fe Kα line, showing lower velocities than the broad line region, whose Hα line observed in polarized light has a FWHM of 3300 km s^{-1} (Oliva et al. 1998).

Bianchi et al. (2001) used *ASCA* and *BeppoSAX* spectra to determine the origin of the strong emission lines that dominate the X-ray spectrum below 2 keV. Spectral fitting showed that these lines are the result of photoionization rather than collisional ionization, suggesting that they are the result of AGN continuum emission shining on cold material. Sambruna et al. (2001) modeled the higher resolution *Chandra* grating X-ray spectra of the nucleus of Circinus and concluded that the soft X-rays are indeed reprocessed nuclear emission from both photoionized and photoexcited plasma. Therefore, at least two distinct reflectors are present in Circinus: one neutral and optically thick responsible for the neutral Fe lines and Compton-scattered continuum, and one photo-ionized, optically thin plasma responsible for the ionized emission lines of lighter elements which dominate the soft X-ray spectra. The soft X-ray emission results were confirmed by Guainazzi & Bianchi (2007), who related the photoionized-emitting plasma to the narrow line region of this AGN and by Massaro et al. (2006), who showed that the nuclear spectrum actually requires three reflectors since the ionized, optically thin spectrum must be produced by at least two different regions.

A weak jet and low power nuclear emission have been observed in 6–20 cm wavelengths in the nucleus of Circinus, where the jet collimation suggests that the emission originates in the AGN. The radio power of the nuclear component, however, is very small, about 10^{38} erg s^{-1} (Elmouttie et al. 1998), which corresponds to 10^{-7} $L_{\rm Edd}$. The *B*-band luminosity is not directly observable but the "blue bump" luminosity estimated from the mid-IR spectral fitting is 4×10^{43} erg s^{-1}, or 20% of $L_{\rm Edd}$. These values place Circinus comfortably in the range of radio-quiet Seyfert galaxies, as shown in the compilation of Sikora et al. (2007). This low radio-power and relatively high accretion rate are similar to the properties of average Seyfert galaxies and consistent with stellar-mass black-hole binaries in the soft state (e.g., McClintock & Remillard 2006).

The proximity of this AGN makes it an ideal target to study in detail both for the properties of the obscurer, as well as for the expected contamination by other sources of emission and scattering outside the nucleus. This contaminating X-ray emission can cause confusion when interpreting the spectra of more distant obscured AGNs.

In this paper, we bring together data with high spatial and spectral resolution and wide energy coverage to constrain the physical parameters of the obscuring matter and quantify the non-nuclear contributions. In Section 2, we describe the main features of the observations performed with each observatory and the reduction procedures. In Section 3, we compare the new *NuSTAR* spectrum to previous observations in similar energy ranges and check its consistency to spectral models fit to the earlier data. We then exploit the timing capabilities of *NuSTAR* to produce the first high-energy, high time resolution lightcurves of Circinus and use the timing properties to further constrain the spectral decomposition. To make an accurate spectral decomposition, we attempt to model all the non-nuclear X-ray sources within the *NuSTAR* extraction region using the higher angular resolution data of *XMM-Newton* and *Chandra*. Toward this end, in Section 4 we analyze the low-energy spectra using *Chandra* to fit separate models to the nuclear spectrum, non-nuclear point sources and the diffuse emission within Circinus. In Section 5, we compare the spectra of the nuclear and brightest point sources using the two *XMM-Newton* observations of Circinus, which cover the longest time span. This is used to look for spectral and flux evolution and isolate the behavior of the different regions. Section 6 presents the joint fits of the galactic and nuclear components of the 2–79 keV spectra using all data sets and in Section 8 we summarize our findings.

2. OBSERVATIONS

We analyze X-ray observations of Circinus obtained by the *NuSTAR*, *Chandra*, *XMM-Newton*, *Swift*, *Suzaku* and *BeppoSAX* observatories between 1998 and 2013. Table 1 summarizes the primary characteristics of each observation used.

2.1. NuSTAR

The *NuSTAR* observatory (Harrison et al. 2013) performed four observations of Circinus between 2013 January 25 and 2013 February 5. The first observation targeted the central AGN on-axis, while the three later observations targeted the ultra-luminous X-ray binary Circinus ULX5 lying 4′ to the south-west of the nucleus (Walton et al. 2013; see Figure 1) such that the AGN was significantly off-axis. Basic observational details are listed in Table 1. The data were reduced using the standard pipeline (NUPIPELINE) from the *NuSTAR* Data Analysis Software (v1.2.0) within the HEASoft package (v6.14), in combination with CALDB v20130509. Unfiltered event lists were screened to reduce internal background at high energies via standard depth corrections and the removal of SAA passages. XSELECT was used to extract data products from the cleaned event lists for both focal plane modules (FPMA and FPMB). Spectra and light curves for the AGN were generated using 100″ radius apertures, while backgrounds were estimated from blank regions free from contaminating point sources on the

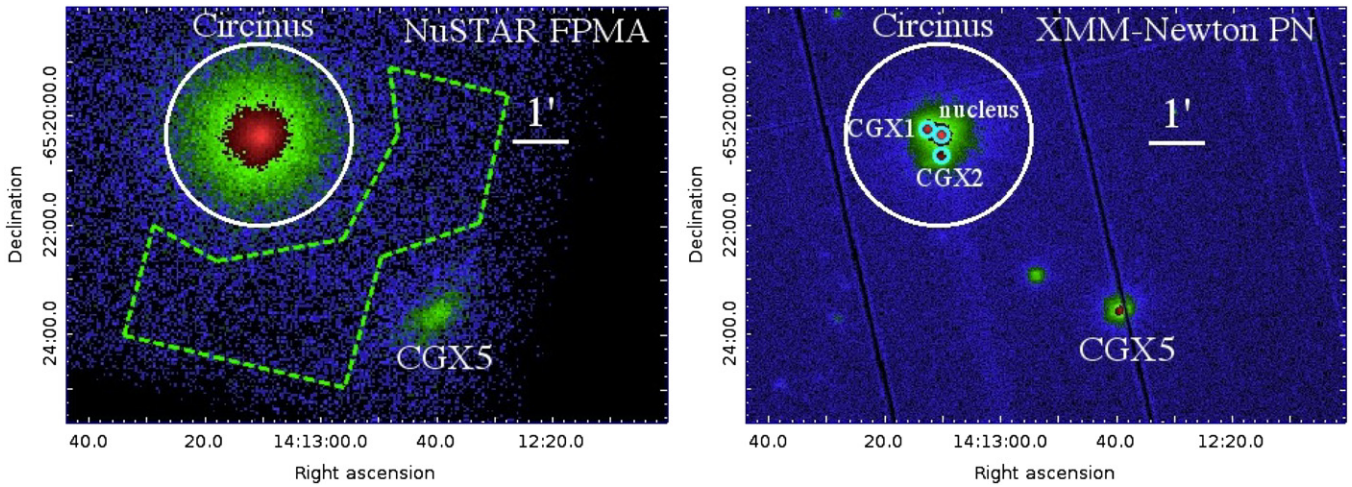

Figure 1. Left: *NuSTAR* FPMA image of Circinus in the 3–79 keV range. CGX5 is visible in the lower right corner. The white and green lines mark the source and background extraction. Right: *XMM-Newton* pn image in the 0.2–10 keV range of the same area. The same source extraction region, marked by the white circle, was used for both observatories. In the pn image, the nucleus plus CGX1 and CGX2 are clearly visible within this source region. The background was extracted from a source free region on the same chip as the source, outside this figure. Both images correspond to the on-axis observations.

(A color version of this figure is available in the online journal.)

Table 1
Summary of Observations

Observatory	Date	Exposure (ks)	ObsID
BeppoSAX	1998 Mar 3	26	5004700200
BeppoSAX	2001 Jan 7	16.7	5004700200
XMM-Newton	2001 Aug 6	103	0111240101
Chandra HETG	2000 Jun 15	68.2	374+62877
Chandra HETG	2004 Jun 2	55.0	4770
Chandra HETG	2004 Nov 28	59.5	4771
Suzaku	2006 Jul 21	140	701036010
Chandra HETG	2008 Dec 8	19.7	10226
Chandra HETG	2008 Dec 15	103.2	10223
Chandra HETG	2008 Dec 18	20.6	10832
Chandra HETG	2008 Dec 22	29.0	10833
Chandra HETG	2008 Dec 23	77.2	10224
Chandra HETG	2008 Dec 24	27.8	10844
Chandra HETG	2008 Dec 26	68.0	10225
Chandra HETG	2008 Dec 27	37.4	10842
Chandra HETG	2008 Dec 29	57.3	10843
Chandra HETG	2009 Mar 1	18.1	10873
Chandra HETG	2009 Mar 4	16.5	10872
Chandra HETG	2009 Mar 3	13.9	10850
Chandra ACIS-S	2010 Dec 17	152.4	12823
Chandra ACIS-S	2010 Dec 24	38.9	12824
NuSTAR	2013 Jan 25	53	60002039002
NuSTAR	2013 Feb 2	18	30002038002
NuSTAR	2013 Feb 3	40	30002038004
XMM-Newton	2013 Feb 3	57	0701981001
NuSTAR	2013 Feb 5	36	30002038006

same detector (see Figure 1). As a cross-check of our "local" background, we also generated a model of the expected background for each FPM for our adopted aperture with NUSKYBGD (Wik et al. 2014). NUSKYBGD uses several user-defined background regions spread over all four detectors in each FPM of *NuSTAR* to simultaneously fit the spectral and spatial dependencies for each background component (e.g., instrumental, focused, and unfocused). Note the angular resolution of *NuSTAR* (FWHM = 18″) is similar to that of *XMM-Newton* and much higher than the other high-energy detectors working in the same energy range as *NuSTAR*: *BeppoSAX* PDS (12′), *Swift* BAT (22′), and *Suzaku* PIN (4.°5).

2.2. XMM-Newton

Circinus was observed with *XMM-Newton* for two long integrations, a 102.5 ks on-axis observation in 2001 and a 57 ks off-axis observation in 2013, targeting CGX5. The observations were made in the Full Window mode using the medium filter. We processed both data sets using SAS version 13.0.0. The events files were filtered to exclude background flares selected from time ranges where the 10–12 keV count rates in the pn camera exceeded 0.6 counts per second in 2001 and 0.8 counts per second in 2013. The remaining good exposure time is 78.4 ks (70.5 ks live time) for the 2001 observation and 41.2 ks (36.5 ks live time) for the 2013 observation.

Three bright central point sources are evident in the pn images, corresponding to the nucleus of the galaxy, the X-ray binary (XRB) CGX1, and the supernova (SN) remnant CGX2, both identified by Bauer et al. (2001). We extracted spectra separately for each of these point sources using 11″ radius circular apertures and for the whole *NuSTAR* region using a 100″ radius aperture centered on the nucleus. Background regions were selected on the same chip where the sources were located.

For the *NuSTAR* aperture, a rectangular background region was selected away from all visible sources. This procedure is equivalent to the *NuSTAR* data case, where all nuclear and contaminating sources are extracted in a single spectrum and the background is selected away from the galaxy. For the small point source extractions we selected background regions immediately surrounding the sources, in order to isolate their spectra from contaminating nuclear and diffuse emission within Circinus. Since all these objects contribute to the *NuSTAR* spectrum, possible variability between epochs is examined in Section 5 to inform the joint fit of the *XMM-Newton* and *NuSTAR* spectra.

We constructed response matrices and ancillary response files using the tasks *rmfgen* and *arfgen* for each epoch and extraction region. The spectra were then binned to contain a minimum of 30 counts per bin.

2.3. Chandra

Circinus has been observed on several occasions with *Chandra* over the past ≈13 yr in both its standard ACIS-S and ACIS-S+HETG configurations. We employ the ACIS-S

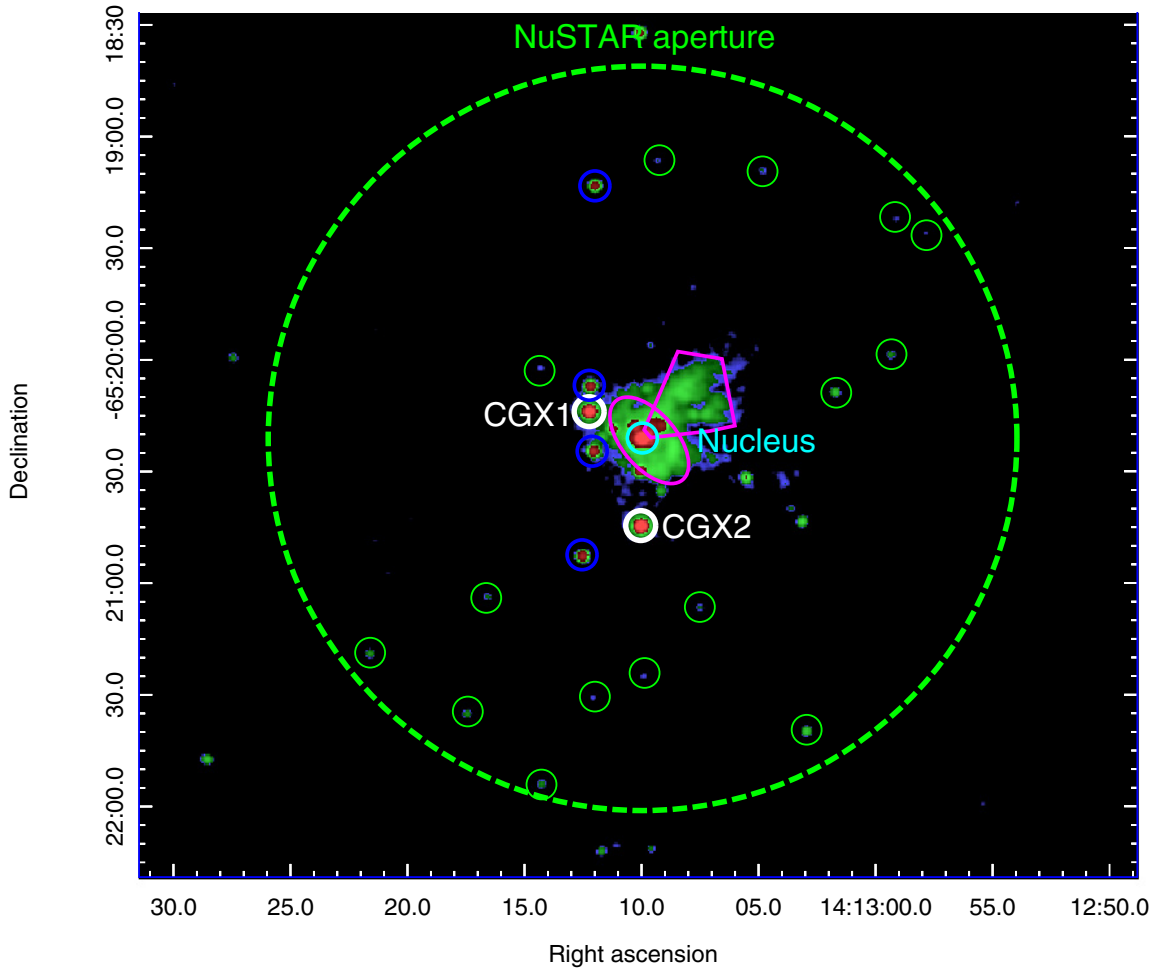

Figure 2. *Chandra* ACIS image of Circinus. The green dashed circle shows the extraction region used for the *NuSTAR* spectra. The point sources modeled individually are marked in white solid lines. The next four brightest point sources are marked in blue and a sample of dim point sources are marked in green. The circles around the point sources represent the 4″ extraction regions used for the *Chandra* spectral modeling. The magenta lines mark the extraction regions for extended emission: an off-center circumnuclear ellipse and the ionization cone. The central region, marked in cyan, was extracted from an annulus that excludes the piled-up central 2″ radius region.

(A color version of this figure is available in the online journal.)

spatially resolved imaging and spectra to model the contribution from contaminating sources around the nucleus of Circinus which fall within the *NuSTAR* extraction region. Unfortunately, the nucleus itself in these data is piled up (60% pileup within 1″–2″), so the nuclear component must be modeled using the HETG grating spectra. The standard ACIS-S configuration provides a spectral resolution of 100–170 eV between 0.4–8 keV, but can suffer from significant photon pile-up for bright sources due to its high spatial resolution and nominal 3.2 s frame time. The addition of the HETG provides an option for higher spectral resolution (60–1000 over the energy range 0.4–10 keV) at the expense of less effective collecting area. The HETG consists of two different grating assemblies, the High Energy Grating (HEG: 0.8–10 keV) and the Medium Energy Grating (MEG: 0.4–8 keV), which simultaneously disperse a fraction of the incident photons from High Resolution Mirror Assembly (HRMA) shells along two dispersion axes offset by 10 degrees to form a narrow X-shaped pattern along the length of the ACIS-S detector. The gratings preferentially absorb soft undispersed photons but let a fraction of higher-energy photons pass through to comprise the HETG 0th order image on ACIS-S.

We retrieved all of the *Chandra* data shown in Table 1 from the *Chandra* Data Archive, and reduced them following standard procedures with the CIAO software (v4.4) and calibration files (CALDB v4.4.6). We reprocessed the data to include the latest calibrations, remove the 0.″5 pixel randomization, and correct for charge transfer inefficiency (CTI). We screened the data with the standard ASCA grade selection, exclusion of bad pixels and columns, and intervals of excessively high background (none was found). Analyses were performed on reprocessed *Chandra* data, primarily using CIAO and custom software including ACIS EXTRACT (v2013-04-29; Broos et al. 2010) for ACIS CCD spectra.

A *Chandra* 0.4–8 keV image of the region around the Circinus AGN is shown in Figure 2. Many different sources appear in the low-energy image within the *NuSTAR* source extraction region, which could potentially contaminate the nuclear emission in the *NuSTAR* band. Thus, to model the nuclear spectrum, we must model all the extra-nuclear sources of emission below 8 keV. To this end, we extracted ACIS-S CCD spectra using standard CIAO tools for several extraction regions as shown in Figure 2 and detailed in Sections 4.2 and 4.3. For simplicity, we only used ObsID s 12823 and 12824 to generate and fit the contamination spectra, as these observations comprise 191.2 ks out of 299.7 ks total normal ACIS-S data (64%), are positioned on-axis, use the entire ACIS-S field of view, and are well-calibrated. The

671.4 ks of HETG 0th order data was not considered due to its significantly larger calibration uncertainties (M. Nowak 2013, private communication).

Since the nucleus is piled up, we modeled it based solely on the higher-order HEG and MEG spectra. HEG/MEG spectral products were extracted from each ObsID using standard CIAO tools using a 6″ full-width HEG/MEG mask in the cross-dispersion direction centered on the AGN. The moderate energy resolution of the CCD detector ACIS-S was used to separate the overlapping orders of the dispersed spectrum. We combined the plus and minus arms to obtain a composite first order spectrum for each grating assembly. We found no obvious variability among the multiple HETG observations, and thus combined all of the spectra and averaged the auxiliary response files (ARFs) into a composite spectrum with 671.4 ks equivalent exposure.

2.4. *Suzaku*

Circinus was also observed by *Suzaku* (Mitsuda et al. 2007) in 2006 for ∼140 ks. We only consider data from the HXD PIN detector, which covers a similar energy range to *NuSTAR*. We reprocessed the unfiltered event files using the HEASOFT software package (version 6.13) and following the *Suzaku* Data Reduction Guide.[26] Since the HXD is a collimating instrument, estimating the background requires individual consideration of the non-X-ray instrumental background (NXB) and cosmic X-ray background (CXB). The response and NXB files provided by the *Suzaku* team were downloaded[27]; here we use the higher quality "tuned" (Model D) background. Spectral products were generated using the HXDPINXBPI script, which also simulates the expected contribution from the CXB using the form of Boldt (1987). Finally, we rebinned the PIN data so that each energy bin had a minimum signal-to-noise ratio (S/N) of 3, sufficient to allow the use of χ^2 minimization. The binned spectra cover the range 15–96 keV. Although ULX5 discussed previously is contained in the HXD field-of-view, the nuclear emission strongly dominates at these energies (Walton et al. 2013).

2.5. *BeppoSAX*

Circinus was observed by *BeppoSAX* on 1998 March 13 (ObsID = 5004700200, and on time ∼26 ks), and on 2001 January 7 (ObsID = 5004700200 and on time ∼16.7 ks). The Phoswitch Detector System (PDS, Frontera et al. 1997) data were calibrated and cleaned using SAXDAS software with the standard method "fixed Rise Time threshold" method for background rejection. The PDS light curves are well known to exhibit spikes on timescales between a fraction of second to a few seconds and usually most counts from spikes are recorded below 30 keV. To screen the PDS data for these spikes we followed the method suggested in the NFI user guide.[28] The PDS spectra were logarithmically binned in the 15–220 keV energy range in 18 channels.

2.6. *Swift*

Since 2004 November, the Burst Alert Telescope (BAT) on board Swift (Gehrels et al. 2004) has been monitoring the hard X-ray sky (14–195 keV). *Swift*/BAT uses a 5200 cm^2 coded-aperture mask above an array of 32768 CdZnTe detectors to produce a wide field of view of 1.4 sr of the sky. Since BAT is continuously observing the sky, a new snapshot image is produced every five minutes for a large number of hard X-ray sources due to its wide field of view and large sky coverage. To study long term source variability we use the publicly available 70 month light curves from *Swift* BAT (Baumgartner et al. 2013). Because of the large energy range of BAT, we are able to test any underlying energy dependence of the light curve. We extracted light curves containing count rates in eight different energy bands: 14–20, 20–24, 24–35, 35–50, 50–75, 75–100, 100–150, 150–195 keV. We also use the stacked 70 month spectra of Circinus.

[26] http://heasarc.gsfc.nasa.gov/docs/suzaku/analysis/
[27] http://www.astro.isas.ac.jp/suzaku/analysis/hxd/
[28] http://heasarc.nasa.gov/docs/sax/abc/saxabc/saxabc.html

3. *NuSTAR* 3–79 keV SPECTRUM

We extracted spectra for *NuSTAR* modules A and B for the on-axis and off-axis observations. The second observation consists of three segments and we initially made a separate spectrum for each. For each epoch, the A and B modules produced largely consistent spectra. The different epochs, however, show differences in the flux at the lowest energies, as shown in Figure 3. Below 5 keV, the normalization of the on-axis and first segment of the off-axis observations are significantly higher than the other two segments of the off-axis observation. The flux of CGX1 is highly variable, as has been shown using spatially resolved *Chandra* data (Bauer et al. 2001). Since this XRB falls inside the *NuSTAR* source extraction region, it is possible that a varying XRB flux is producing the observed differences in the *NuSTAR* spectra. Based on the spectral extraction of CGX1 in the *XMM-Newton* data presented in Section 5, CGX1 does appear to be solely responsible for the observed variability. The differences between the different *NuSTAR* spectra are consistent with a changing normalization of the absorbed power law component that will be used to model CGX1 below in Section 4.2.

The 3–5 keV flux measured for the four segments is 4.1×10^{-12} erg s^{-1} cm^{-2} for the first two and $3.4–3.2 \times 10^{-12}$ erg s^{-1} cm^{-2} for the second and third segments, respectively. The CGX1 flux would have to change by 6.9×10^{-13} erg s^{-1} cm^{-2} to make up for the differences in the spectrum. To account for this difference, in the on-axis *NuSTAR* observation and the first segment of the off-axis observation the power law normalization of CGX1 should be 6.87×10^{-4} photons keV^{-1} s^{-1} cm^{-2} at 1 keV higher than in the second and third off-axis observations. This difference is incorporated in the joint fits of Section 6 when combining the spectra of the on-axis *NuSTAR* observation with the 2013 pn spectrum, which coincides in time with the second segment of the off-axis *NuSTAR* observation.

Once this power law normalization difference is accounted for, small differences remain around the 6.4 keV emission line, which shows a stronger red wing in the off-axis spectra. Since the energy calibration is less certain at off-axis positions we will use only the on-axis spectra. Above 8 keV there are no significant differences between the four different epochs. Figure 3 shows all the *NuSTAR* spectra divided by the same power law with $\Gamma = 0.889 \pm 0.003$ and norm $= (1.30 \pm 0.01 \times 10^{-3})$ photons keV^{-1} s^{-1} cm^{-2} at 1 keV, showing that the spectra are highly consistent at most energies and there are no other measurable fluctuations in the spectral shape or flux of the different epochs.

We compared simultaneous observations of Circinus with *NuSTAR* and *XMM-Newton* to measure any flux calibration differences. We selected *NuSTAR* events over the time range where the off-axis observation overlapped with the 2013

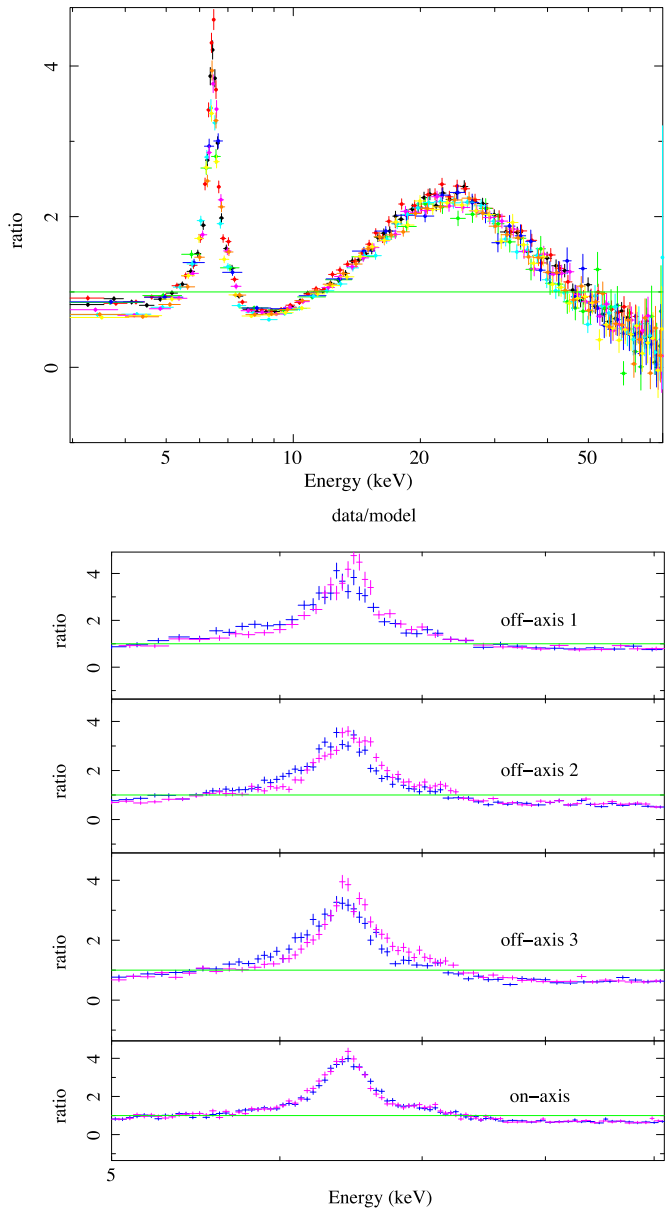

Figure 3. Top: ratio of all *NuSTAR* spectra to a power law of slope 0.89 and normalization of 1.3×10^{-3} photons keV^{-1} s^{-1} cm^{-2} at 1 keV; both modules and the four exposures produce consistent spectral shapes and normalizations, except for details visible at low energies, where the spectra of FPMA and FPMB of the first two exposures (black, red, green, blue) are slightly higher than the spectra of the last two exposures (cyan, magenta, yellow, and orange). Bottom: same spectra as above focusing in on the Fe K line region. Blue points correspond to FPMA and magenta to FPMB, with each panel showing a different ObsID. The on-axis observations produce the most consistent spectra between the modules and have sufficient counts for accurate spectral fitting in this energy range.

(A color version of this figure is available in the online journal.)

XMM-Newton observation. The resulting *NuSTAR* spectra were fitted together with the 2013 pn spectrum using the same spatial extraction region, over the 3–10 keV energy range where the observatories overlap. Fitting both spectra with a power law of equal slope and free normalization gives normalizations of $(5.05 \pm 0.13) \times 10^{-4}$ for pn, $(6.08 \pm 0.20) \times 10^{-4}$ for *NuSTAR* FPMA and $(6.23 \pm 0.20) \times 10^{-4}$ for FPMB. FPM A and B are consistent within the statistical error, while they are both about 20% above the pn value. For this reason we will multiply the models by a constant factor of 1.2 when fitting them to *NuSTAR*

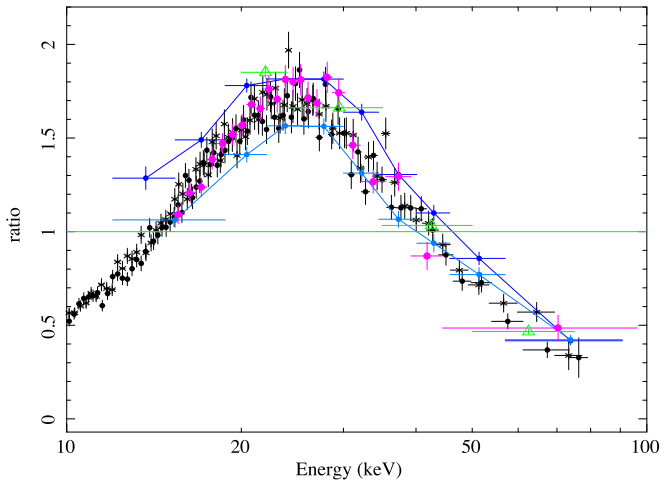

Figure 4. Residuals of Circinus spectra taken with different observatories to the same power law model, where only the normalizations were corrected for known mismatches in the response of the instruments. The on-axis *NuSTAR* spectra are plotted in black (FPMA in circles, B in stars), two different *BeppoSAX* PDS observations are plotted in blue and light blue, *Suzaku* PIN data are plotted in magenta, and *Swift* BAT in green triangles. The spectra were binned to similar significance levels. The data are broadly consistent in flux and shape. The difference between the *BeppoSAX* spectra is discussed in the text.

(A color version of this figure is available in the online journal.)

spectra in the joint fitting described in Section 6. We note that this constant cross-calibration factor has changed in the latest version of the *NuSTAR* extraction software to a value of ∼1.

3.1. Comparison to Previous Hard X-Ray Observations

Circinus had been observed previously above 10 keV by *BeppoSAX* in 1998 and 2001 (Matt et al. 1999; Bianchi et al. 2001, 2002) and in 2006 by *Suzaku* (Yang et al. 2009). Figure 4 compares the observations from the three satellites, showing the ratio of their spectra to the same power law model, where only the normalizations were shifted for known mismatches in the response of the instruments. The model normalization has been shifted upward by 20% for *NuSTAR* spectra, as discussed above. The *Suzaku* PIN normalization has been shown to be 16% too high when compared to the XIS;[29] we therefore also corrected its model normalization up by this amount. The PDS normalization has been shown to be too low by 20% (Grandi et al. 1997) so we multiplied the model normalization by 0.8 when applied to these data. The 70 month average BAT spectrum model was rescaled by a cross-calibration coefficient of 0.95, to match the *NuSTAR*/*Suzaku* spectra.

With these corrections to the normalizations, the spectra are very similar, with *Suzaku* PIN and *Swift* BAT spectra being fully consistent with *NuSTAR*. The two *BeppoSAX* observations, one lower and one higher than the other spectra, were compared by Bianchi et al. (2002). These authors ascribe the large change in flux between observations to variations of CGX1, although the brighter ULX5, 3′ away from the nucleus, might also contribute to this spectrum. Even if a 2′ extraction region was used, ULX5 is bright enough and variable, such that it could have contaminated the nuclear spectrum given the broad point-spread function (PSF) of the *BeppoSAX* PDS. The alternative is that the *BeppoSAX* PDS observation indeed caught a rare, less obscured, glimpse into the central engine that has not been reproduced since (see Section 7). Repeating the extraction with

[29] ftp://legacy.gsfc.nasa.gov/suzaku/doc/xrt/suzakumemo-2008-06.pdf

a 1′ radius reduced the nuclear variation to a level where it was no longer significant (Bianchi et al. 2002). ULX5 has a softer spectrum than the nucleus (Walton et al. 2013), so the "soft excess" visible in the *BeppoSAX* spectra is consistent with this potential contamination. A further probable cause for this difference in flux between the *BeppoSAX* observations is the background subtraction method required by the low-spatial resolution of PDS, whereby a blank field is used to estimate the background contamination. Low-flux sources in this field can cause the background to be overestimated and therefore the source flux to be underestimated. Considering these limitations, we do not raise further concerns about the discrepancy between both *BeppoSAX* spectra and the *NuSTAR* spectrum.

We note that more confidence should be placed in the *NuSTAR* data, which offer higher quality high-energy spectra than *Suzaku* PIN and *BeppoSAX* PDS due to the focusing nature of the telescope. The large concentration factor leads to greatly reduced internal background levels, higher S/N spectra, and less uncertainty from nearby source contamination. Once convinced that the *NuSTAR* spectra are compatible with previous observations, we will base our final spectral modeling above 10 keV in Section 6 largely on the *NuSTAR* data although we also incorporate the *Swift* BAT data to better constrain the highest energies.

4. DETAILED BROADBAND FITTING: SPECTRAL COMPONENTS IN THE 0.8–8 keV RANGE

The high spatial resolution images of *Chandra* ACIS show a number of point sources as well as extended X-ray emission within the 100″ region used to extract the *NuSTAR* spectrum. In this section, we model the nuclear emission and assess the contribution of these contaminants to the nuclear flux.

4.1. Nuclear Spectrum

The HEG and MEG are the only spectra with sufficient spatial resolution to model the central 3″ alone, since the ACIS data are strongly piled up in this region. These spectra, shown in the top panel in Figure 5, have two distinct features: a forest of narrow emission lines at low energies and, above 2 keV, a hard power law with prominent emission lines at 6.4 and 7.1 keV. The spectrum above 2 keV is characteristic of Compton-scattered and fluorescent lines produced by reflection of the AGN continuum off neutral matter.

Sambruna et al. (2001) fitted 60 ks of this *Chandra* HETG observation and interpreted the 1–8 keV spectrum as two distinct reflection components, one from ionized material and one from nearly neutral material. The soft X-ray emission lines are largely produced by the ionized medium. Line intensities correspond to a photoionized and photoexcited medium rather than collisionally ionized gas. Guainazzi & Bianchi (2007) analyzed reflection grating spectrometer (RGS) spectra of Circinus below 1 keV finding narrow radiative recombination continua (RRC), which require a low gas temperature of a few eV and indicate that the gas is in photoionization equilibrium. The neutral reflection found by Sambruna et al. (2001) is highly concentrated toward the center of the galaxy and is responsible for the strong Fe Kα and Kβ lines as well as a hard reflection continuum.

We initially model the Compton reflection and Fe fluorescent lines with `MYTorus` scattered and line components. The most prominent emission lines correspond to the Kα and Kβ transitions of neutral Fe and are calculated consistently with the Compton-scattered component. These lines are the only

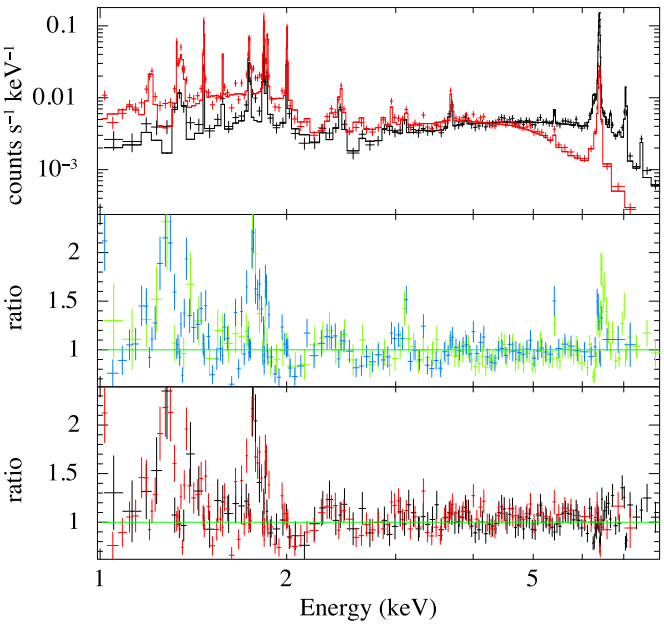

Figure 5. Nuclear spectrum: HEG (black) and MEG (red) spectra extracted from the central 3″ radius region, fitted with `MYTorus` scattered+lines plus the Gaussian lines identified in Sambruna et al. (2001). The ratio to this model is shown in the middle panel. The spectrum above 2 keV was fit with additional Gaussian lines as described in the text. This final model is fit to the spectra in the top panel and its data/model ratios are shown in the bottom panel.

(A color version of this figure is available in the online journal.)

ones modeled by `MYTorus`, although neutral lines from other elements should also be present at a considerably lower flux level. The cold photoionized medium is simply modeled as the Gaussian lines reported in Table 1 of Sambruna et al. (2001), over a power law representing reflection of the nuclear continuum. The RGS spectrum of Circinus presented by Guainazzi & Bianchi (2007) shows that lower energy emission is highly dominated by narrow emission lines and therefore is not helpful in constraining the behavior of an underlying scattered or Compton-scattered continuum component. Given the low count rate of our spectra at the lowest energies, the resolution of our binned-HETG spectra cannot resolve these low-energy lines, so we will restrict our analysis to energies above 1 keV. The lowest energy line reported by Sambruna et al. (2001) is at 1.2 keV. Below this energy, many closely separated transitions of Fe XIII through Fe XXIV, plus Na lines are unresolved by our data and resemble continuum emission. We model these collectively as two broad (FWHM = 0.01 keV) Gaussian lines at 1 and 1.1 keV. Allowing the rest of the line widths and all normalizations to vary, we obtain a $\chi^2_{\rm red} = 1.48$ for 1287 dof. The overall shape of the spectrum is well reproduced but residuals remain around most of the emission lines. Many of the emission lines reported by Sambruna et al. (2001) originally modeled several transitions together. Our higher S/N spectrum shows many narrow cores over these moderately broad lines ($\sigma = 0.01$ keV). Our aim is to constrain the continuum components that contribute to higher energies and not to derive the gas properties from line diagnostics. Therefore, we fixed the power law slope and normalization from this fit and restrict further analyses to energies above 2 keV where the lines are only a minor contribution to the flux. In the 2–8 keV range this model produces $\chi^2_{\rm red}$ =1.25 for 857 dof. We also included lines not reported in Sambruna et al. (2001), including a 7.4 keV (Ni Kα, Molendi et al. 2003), 6.55±0.21 keV (blend of the Fe XXV triplet, Bianchi et al. 2002)

and 3.108 ± 0.002 keV (S XVI Kβ), 5.41 ± 0.01 keV (Cr Kα) and 2.18 ± 0.02 keV (Si XIII Kβ) 5.885 ± 0.005 (Cr XXIV Kα), modeled as narrow Gaussians with their widths tied. Repeating the fit with free normalization of these lines and of the MYTorus component improves the fit significantly to $\chi^2_{\rm red} = 1.04$ for 852 dof.

Although this fit is already good, the residuals show striking structure around the Fe Kα line, where the line core is underpredicted and the Compton shoulder is overpredicted. However, as the Fe line emission is spatially extended, the nuclear spectrum has contamination from neighboring energy bins due to incorrect spatial versus. energy assignments along the dispersion direction. We estimate that this spatial/spectral energy separation degeneracy leads to an overall broadening of emission lines by 0.1–0.2 keV (effectively the energy resolution of ACIS-S) and an overestimate of ~20% in the line flux around 6.4 keV. We included narrow Gaussian lines to simulate this contamination of the strongest lines at 6.4 and 7 keV in the nuclear spectrum. Finally, fitting the Compton-scattered component together with these lines produces a $\chi^2_{\rm red} = 0.97$ for 851 dof.

In addition to the MYTorus Compton scattering component, we have included the transmitted AGN continuum using the MYTorus zero-order model, since we are looking directly in the direction of the AGN. Given the large optical depth toward the nucleus, this transmitted component does not make a notable contribution in the *Chandra* band, but might contribute significantly to the spectrum at higher energies. As a first approach, we tied all the MYTorus components—Compton-scattered, transmitted spectrum, and Fe lines—to have the same $N_{\rm H}$, inclination angle, intrinsic power law slope, and normalization, which corresponds to a uniform torus geometry. Since the model already produces a very good fit at energies where the Compton-scattered component dominates, the fit does not improve significantly by freeing these constraints.

Previously, Molendi et al. (2003) modeled the 4–12 keV nuclear spectrum using the pn data from the first *XMM-Newton* observation. Their analysis of the Fe line, its Compton shoulder and the depth of the Fe edge indicated that the same Compton thick matter was responsible for the line-of-sight absorption and for the volume-averaged Compton scattering. They therefore identified the reflector with the absorber, possibly corresponding to the molecular torus. The consistency between their parameters pointed to a fairly uniform torus. Their best-fitting model produced an intrinsic power law slope $\Gamma = 1.9$ and Fe abundance of 1.2 with respect to solar. In our approach, the Compton-scattered component is modeled with MYTorus instead of pexrav, which does not produce large differences below 10 keV and is not very sensitive to the incident power law slope in this energy range, making this value of Γ acceptable in our fits as well. The Fe abundance is also consistent with our findings, since the MYTorus Fe lines are calculated using solar abundances and we fix the scaling between Compton-scattered and Fe lines to 1.

The parameters of the Compton scatterer are not well constrained in this energy range. Allowing only the $N_{\rm H}$ and normalization of MYTorus to vary, together with the normalization of the scattered power law, the best-fitting values for MYTorus components are $N_{\rm H} = (9.4 \pm 7.7) \times 10^{24}$ cm^{-2}, normalization of 0.21 ± 0.06 photons keV^{-1} s^{-1} cm^{-2} at 1 keV for the Compton-scattered power law, and $(1.5 \pm 0.4) \times 10^{-4}$ photons keV^{-1} s^{-1} cm^{-2} at 1 keV for the scattered power law normalization. Higher energy data are necessary to constrain further the Compton scattering component.

4.2. Point Sources

After the nucleus, the brightest point sources within 100″ of the nucleus of Circinus are CGX1, a bright X-ray binary, and CGX2, a young supernova remnant. Both were previously identified and characterized by Bauer et al. (2001). We extracted their ACIS 0.5–8 keV spectra using circular regions 4″ in radius. The next four sources ranked in flux were extracted with the same criteria and combined to produce a spectrum representative of lower luminosity point sources. A further sample of 15 dimmer point sources were extracted and modeled together. These regions are marked in Figure 2.

The best known nuclear contaminants are CGX1 and CGX2. We modeled the first one, an XRB, with a simple absorbed power law (phabs*power law) which produced a reasonably good fit with $\chi^2_{\rm red} = 1.1$ for 394 dof. The phabs $N_{\rm H} = (1.03 \pm 0.03) \times 10^{22}$ cm^{-2} is slightly higher than the Galactic value of 3×10^{21} cm^{-2} (Freeman et al. 1977), indicating absorption in the host galaxy. The power law slope is $\Gamma = 1.80 \pm 0.04$ (norm $= 2.77 \times 10^{-4}$ photons keV^{-1} s^{-1} cm^{-2}), typical of XRB slopes. No strong emission lines are evident.

The spectrum of CGX2 shows strong emission lines, most clearly He- and H-like Fe at 6.7 and 6.95 keV plus several emission lines in the soft X-rays. This spectrum is produced by the supernova ejecta, composed of hot, optically thin gas of non-solar abundances being ejected at velocities of up to 10,000 km s^{-1}. The gas is not in ionization equilibrium and covers a wide range in temperatures which we crudely model using several thermal plasma components. The simplest model that produces a reasonable fit ($\chi^2_{\rm red} = 1.19$ for 415 dof) was three Mekal components with temperatures of 0.09 ± 0.02, 1.09 ± 0.03, and 9.15 ± 0.38 keV, abundances in units of Solar abundance of 0.5 (frozen) for the lowest temperature phase and 7.5 ± 0.8 for the other two and redshifts of 0.08 ± 0.04, -0.0066 ± 0.0014, and -0.0028 ± 0.0018. All these components are under a layer of cold absorption modeled by phabs with $N_{\rm H} = 2.2 \times 10^{22}$ cm^{-2}.

The remaining point sources were fitted together in groups to improve their signal-to-noise ratio. First the third to sixth brightest were modeled in the same way as CGX1, producing similar fit values. Their combined spectrum are well fitted by an absorbed power law of slope $\Gamma = 1.8$ and column density $N_{\rm H} = 5 \times 10^{21}$ cm^{-2}. The joint normalization is 1.5×10^{-4} photons keV^{-1} s^{-1} cm^{-2}, a factor of 2 lower than that of CGX1. The next 15 fainter point sources together produced a steeper slope and lower normalization so their contribution is unlikely to be an important source of contamination in the *NuSTAR* band.

The predicted contribution of high-mass X-ray binaries (HMXBs) was also calculated from the measured star formation rate for the entire Circinus galaxy, which has been estimated to be between 0.2 and 6 $M_\odot$ yr^{-1} (e.g., Grimm et al. 2003; Roy et al. 2008). Using the scaling relation of Lehmer et al. (2010) and a distance of 4.2 Mpc, the predicted 2–10 keV flux produced by HMXBs is $(0.4–5.3) \times 10^{-12}$ erg s^{-1} cm^{-2}. This level of HMXB contribution is plotted in gray solid lines in Figure 6 along with the various spectra of the resolved point sources highlighted above. Both CGX1 and CGX2 alone fall within the expected range, so together they can represent the majority of the point source contribution to the spectrum below 8.0 keV. We are therefore confident that unresolved point sources will not contaminate significantly more than what is already accounted for in our composite model.

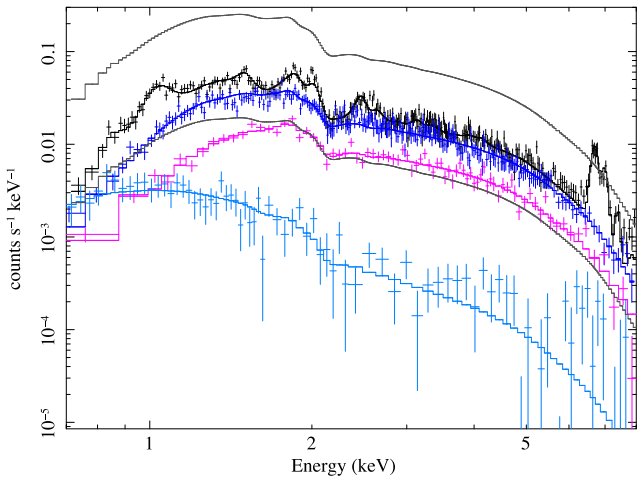

Figure 6. *Chandra* ACIS spectra and models of point sources within the *NuSTAR* extraction region: CGX1 (dark blue), CGX2 (black), the next 4 brightest point sources (magenta), and a sample of 15 dimmer point sources (light blue). All of these sources have steep spectra ($\Gamma \sim 1.8$) so they will not contaminate the >10 keV spectra significantly. The supernova remnant CGX2 contributes the majority of the ionized Fe emission (6.7 and 6.9 keV) in the *NuSTAR* aperture. The gray lines mark the lower and upper limits of the expected contribution from HMXBs in the entire galaxy, modeled as power laws of $\Gamma = 1.8$ under a cold absorber of $N_{\rm H} = 1 \times 10^{22}$ cm^{-2}.

(A color version of this figure is available in the online journal.)

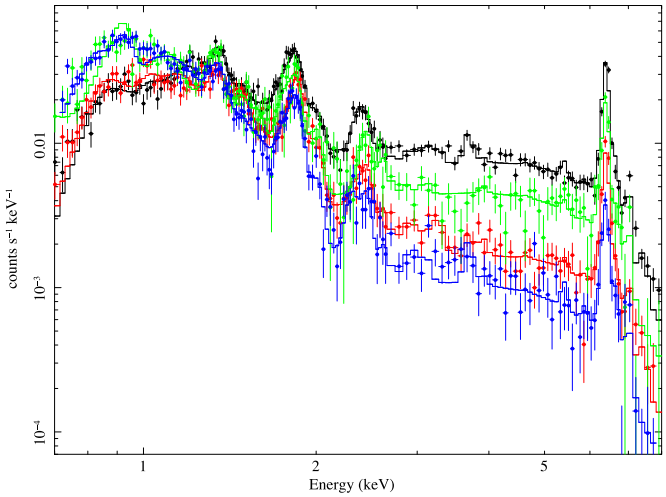

Figure 7. *Chandra* ACIS spectra and models of the diffuse emission regions within the *NuSTAR* extraction radius: center (black), circumnuclear ellipse (red), ionization cone (blue), and everything else (green). All regions contain soft X-ray emission lines and a strong reflection continuum together with prominent neutral Fe K lines.

(A color version of this figure is available in the online journal.)

4.3. Diffuse Emission

Diffuse emission can be seen mainly around the nucleus of Circinus and at the location of the ionization cone, though dimmer emitting regions exist throughout the galaxy. This emission is produced by a combination of hot gas created from the starburst and AGN jets (Mingo et al. 2012) as well as AGN emission reflected off neutral (e.g., Smith & Wilson 2001) and photoionized material (Sambruna et al. 2001).

We extracted spectra for four distinct regions: the ionization cone region marked in Figure 2; a circumnuclear ellipse excluding the central 3″ which corresponds to the nucleus; nuclear emission within 3″ but excluding the innermost 2″ radius, which is significantly piled-up, and all the remaining area enclosed in the *NuSTAR* aperture (100″ radius) excluding the diffuse and point source regions discussed above.

The ionization cone, circumnuclear region, central annulus, and everything else make similar contributions to the 0.5–8 keV flux. Their spectra and best-fitting models are plotted in Figure 7. All the spectra of extended regions show a soft component with emission lines plus a hard continuum component above 2 keV and strong neutral Fe lines at 6.4 and 7 keV, characteristic of reflection off cold material. This last component is likely associated with a Compton hump extending to higher energies.

A simple fit to the four spectra was performed using the nuclear high-resolution spectrum model described in Section 4.1. We allowed the normalization of the Compton-scattered component and the scattered power law plus soft lines to vary independently to account for different ratios of optically thin to optically thick reflection. We also added one thermal component to account for the hot gas (shocked and starburst related) emission. This produced reasonable fits, which were improved by allowing the normalizations of the low energy emission lines to vary as well. The resulting models are plotted as lines in Figure 7. Note that in the Compton-scattered component (continuum plus Fe lines) only the normalization was allowed to vary, therefore the equivalent width of the Fe lines was assumed to be the same in all regions. This produced a good description of the data.

Since the Compton-scattered and power-law spectral shapes were fixed, it is possible to directly compare their contributions to the flux from the model normalization. The normalization of the Compton-scattered component is 1.5%, 3.4%, 14.4%, and 7.8% of the nuclear value in the ionization cone, circumnuclear region, central annulus, and everything else, respectively.

It is important to note that the Compton-scattering component in the contamination model is most likely produced by the AGN from reflection at large distances. However, the Compton-scattering parameters are not well constrained by the 0.6–8.0 keV data so they will be allowed to vary in the joint fit to *Chandra*, *XMM-Newton* and *NuSTAR* spectra.

4.4. Contamination Model

The aim of the previous sections was to model the spectral shape and flux of contaminating sources below 8 keV and predict their contribution above this energy in the *NuSTAR* band. We found that the largest contributions above 8 keV are produced by the Compton-scattered flux from diffuse emission regions and, to a lesser extent, the thermal emission from the hottest gas in CGX2 and the power law spectra from X-ray binaries. We collected these components into a simplified model for the contamination, composed of a thermal plasma component to model all the thermal emission of the diffuse regions, all the thermal components of CGX2 fixed, one Compton-scattered continuum plus Fe lines to model an average of all the off-nuclear neutral reflection, one absorbed power law with $\Gamma = 1.8$ for all the point-source emission (with fixed normalization), and another soft power law for the AGN scattered emission.

The sum of the nuclear component fit to the HETG data and the contamination fit with ACIS data should account for the total flux within the *NuSTAR* aperture. The *XMM-Newton* pn spectrum from 2013 extracted from the same region was fitted with the sum of both components with all emission lines above 6 keV in the model shifted up by 40 eV, including the Compton-scattered Fe lines modeled with `MYTorus` in the nuclear and contamination components. The cross-calibration between *XMM-Newton* pn and *Chandra* ACIS has been calculated by Nevalainen et al. (2010) among others. These authors find a flux ratio between pn and ACIS

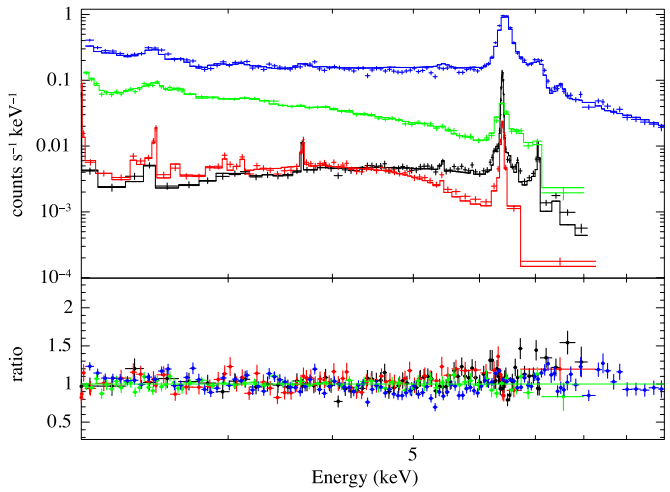

Figure 8. Joint fit of the low energy data: *Chandra* HEG (black) and MEG (red) fitted with the nuclear model, ACIS (green) represents the contaminating sources in the galaxy and *XMM-Newton* pn (blue), is modeled as the sum of all the nuclear and contamination models. The normalization of the variable CGX1 was allowed to vary between the ACIS contamination spectrum and the pn full spectrum and line energies were shifted by 40 eV in the pn spectrum to account for calibration differences. All other model parameters are the same for all data sets.

(A color version of this figure is available in the online journal.)

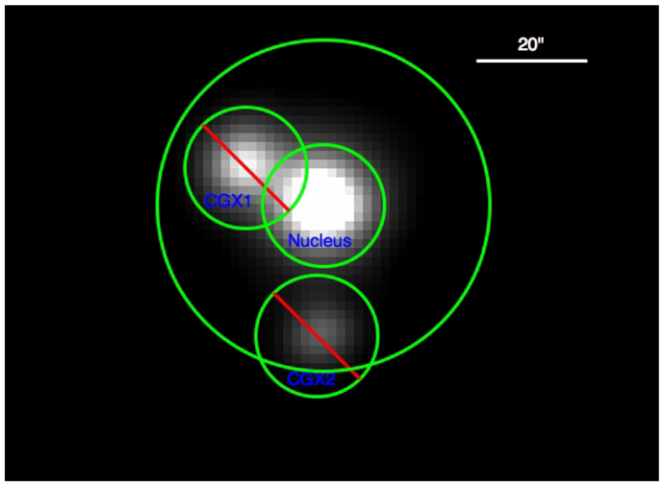

Figure 9. *XMM-Newton* pn image of Circinus. The central green circle 11″ in radius marks the extraction region for the nuclear spectrum while the background were taken from the larger annulus shown, after removing the regions shown around CGX1 and CGX2. Similar source and background regions were used for CGX1 and CGX2 spectra, centering the annuli on the source of interest and removing the other two sources from the background area. For CGX1 the extraction radius was changed to 7.″5 to reduce the contamination from the nucleus.

(A color version of this figure is available in the online journal.)

of 0.81–1 for galaxy cluster measurements in the 2–7 keV, where the range in cross-calibration factors is much larger than the statistical error on each fit. We allow for overall normalization differences in a similar range. Freezing all the parameters except an overall normalization factor we model the pn spectrum as the sum of the contamination and nuclear spectral models. Since our contamination spectrum has at least one variable source and the spectra are not simultaneous, we further allow the normalization of CGX1 to vary in the pn spectrum. CGX1 is responsible for approximately a constant fraction of the continuum contamination flux in this energy band so a varying XRB flux can emulate a different cross-calibration except in the regions where the emission lines dominate the flux. Considering these two free normalization factors for the pn spectrum only, we fit the three data sets simultaneously, allowing only the normalization of the Compton-scattered component to vary for all data sets together. This joint fit produces $\chi^2_{\rm red} = 1.13$ for 1069 dof, in the 2–8 keV (2–10 keV for pn) and is shown in Figure 8. Inspection of the residuals shows a small but systematic difference between the *Chandra* and pn spectra, where the pn flux drops steadily with respect to the other instruments by about 10% throughout the energy band. Similar trends have been found at lower energies by Nevalainen et al. (2010). This difference between instruments produces most of the residuals. The best-fitting cross-calibration coefficient is 1.02 ± 0.01 and the normalization of the CGX1 power law is $(1.65 \pm 0.5) \times 10^{-4}$ photons keV^{-1} s^{-1} cm^{-2} at 1 keV, which represents a drop of about a factor of two of this component in the pn data compared to the ACIS spectrum. In the following fits, we will freeze the pn CGX1 normalization and cross-calibration coefficient to these best-fitting values.

5. LONG-TERM SPECTRAL EVOLUTION OF THE BRIGHTEST SOURCES IN CIRCINUS: *XMM-Newton* OBSERVATIONS

The *XMM-Newton* observations of Circinus are separated by 12 yr with the second observation taken simultaneously with one of the two *NuSTAR* exposures. We use these data to investigate possible long-term variations in the X-ray flux and spectrum and use the simultaneous observations to estimate the cross-calibration offset between the observatories.

The lower spatial resolution of *XMM-Newton* compared to *Chandra* allows us to distinguish only three separate sources within the *NuSTAR* aperture: the nuclear region and the point sources CGX1 (XRB) and CGX2 (supernova remnant). We extracted spectra for these three regions using 11″ aperture radii for the nucleus and CGX2, and a 7.″5 radius aperture for CGX1 to reduce the strong contamination of nuclear flux in this region. The background region for the nuclear spectrum is shown in Figure 9 and similar regions were selected around the other two sources. The resulting spectra for 2001 (blue) and 2013 (magenta) are shown in Figure 10.

As expected, the nuclear component displays the smallest amount of variability. This spectrum was fitted with `MYTorus` scattered plus line emission, two components of hot gas and additional broad Gaussian lines, similar to the model used for the HEG/MEG nuclear spectrum described above. Allowing only an overall multiplicative factor to vary between both epochs, the best-fitting factor equals 1.02 ± 0.008. This error range only represents the statistical error and does not incorporate small differences in response of the instrument over the time period or the different source positions on the CCD. The measured 0.5–10 keV fluxes were 1.19×10^{-11} erg s^{-1} cm^{-2} in 2001 and 1.22×10^{-11} erg s^{-1} cm^{-2} in 2013. The largest discrepancy between the epochs appears around the strong emission lines, where a small shift in the line energies is evident. We estimated the line centers by fitting the 5–8 keV region of both spectra with a simpler model consisting of a power law with an edge at 7.1 keV and three Gaussian lines, originally at 6.4, 7.0 and 7.4 keV in the rest frame, corresponding to neutral Fe Kα and Kβ and Ni Kα, respectively.

The 2001 spectrum produced line energies of 6.400 ± 0.001, 7.054 ± 0.030, and 7.460 ± 0.010 keV, consistent with the expected values for these lines. The 2013 spectrum, on the other

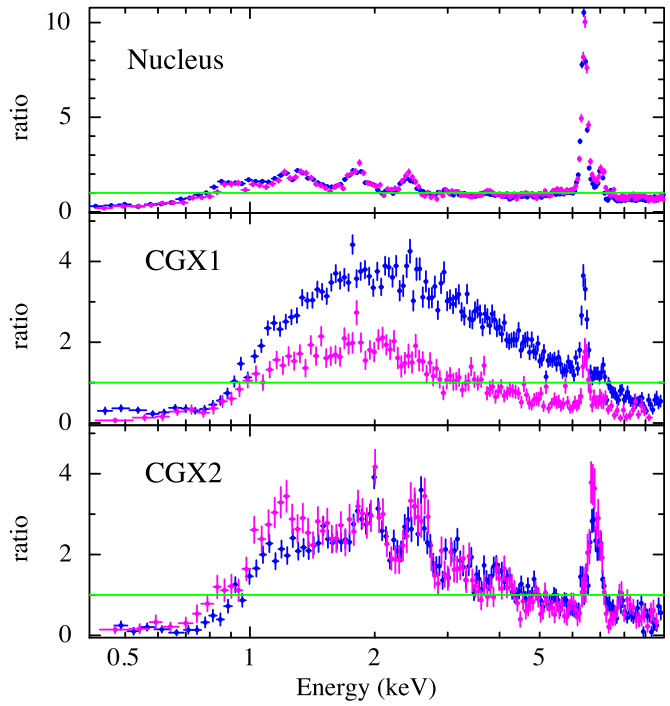

Figure 10. Comparison of 2001 (blue) and 2013 (magenta) spectra of the nuclear region, the XRB CGX1, and the supernova remnant CGX2 using *XMM-Newton* pn data. For each object, both epochs have been fitted with the same power law, so that the ratios plotted highlight the evolution of each spectrum. The strongest evolution is shown by CGX1, where the flux dropped by a factor of 2. The nuclear flux and spectral shape has remained essentially constant. CGX2 shows a small drop in gas temperature and a very small change in flux.

(A color version of this figure is available in the online journal.)

hand, produced consistently higher energies for the lines, at 6.434 ± 0.002, 7.145 ± 0.013, and 7.490 ± 0.020 keV. This is an instrumental effect produced by the energy calibration at off-axis positions on chip 4 of the pn camera (M. Stuhlinger 2013, private communication). The Metal Oxide Semi-conductor CCD array spectra extracted for the same observation have the Fe Kα and Kβ lines at the correct rest-frame energies, confirming that the pn lines are shifted to higher energies by calibration effects. The shift is small but important for the joint spectral fits described below; given the strength of these lines and the high S/N of the *XMM-Newton* data, this discrepancy has a large effect on the fit statistics. Therefore, in the joint fit we shift the model lines by 40 eV when considering the pn spectrum, while keeping all other parameters tied between observatories.

The largest variation between epochs is for the XRB CGX1 with an overall decrease in 0.5–10 keV flux by a factor of 2.3, from 4.14×10^{-12} erg s^{-1} cm^{-2} to 1.79×10^{-12} erg s^{-1} cm^{-2}. We fitted this spectrum with a power law of fixed $\Gamma = 1.8$ under a cold absorber modeled with `phabs` and two Gaussian lines at 6.4 and 7 keV. The power law normalization drops by a factor of 2.7 from $1.106 \pm 0.019 \times 10^{-3}$ in 2001 to $4.116 \pm 0.018 \times 10^{-4}$ photons keV^{-1} s^{-1} cm^{-2} at 1 keV in 2013. A small change in column density is required by the fit, from 1.1×10^{22} cm^{-2} to 7.8×10^{21} cm^{-2}. As seen in the ACIS spectrum of CGX1, the XRB itself does not produce emission lines, so the Fe Kα and Kβ lines observed in its pn spectrum must be contaminated by the nucleus and diffuse emission. Any contamination from the reflection continuum that accompanies these lines is incorporated into the power law component of the fitted model, so the actual flux change of CGX1 alone might be larger than measured.

The supernova remnant CGX2 evolved to lower temperatures. When modeled by three hot gas components under cold absorption using MEKAL and `phabs` models as above, the temperatures change from 10.8 ± 0.5, 1.2 ± 0.1 and 0.12 ± 0.03 keV in 2001 to 8.3 ± 0.5, 0.9 ± 0.5 and 0.13 ± 0.01 keV in 2013. The integrated 0.5–10 keV flux changed by 3%, from 1.51×10^{-12} erg s^{-1} cm^{-2} to 1.56×10^{-12} erg s^{-1} cm^{-2}.

The analysis above shows that we can expect changes in the contaminating sources within the *NuSTAR* aperture at different epochs. The observations performed with *NuSTAR* and *Chandra* are closer in time to the second *XMM-Newton* observation, so we will use this last *XMM-Newton* observation to make the joint spectral fits. We bear in mind, however, that the energy calibration of the 2013 pn spectrum is shifted to higher energies by about 40 eV at 6 keV and that the normalization of CGX1's contribution to the contamination must be allowed to vary between observations.

6. BROADBAND SPECTRAL FITTING

Having modeled the nuclear and contamination spectra in the 2–8 keV band, we combine these components to fit the 2–79 keV band. We use the models fit to the nuclear HETG spectra and the contamination model fit to the ACIS spectrum. These two models together should reproduce the *XMM-Newton* pn and *NuSTAR* spectra extracted from the entire 100″ radius circular region centered on the AGN. For the joint fit we use the *Chandra* spectra together with the 2013 *XMM-Newton* pn and the on-axis 2013 *NuSTAR* data observation. These last two instruments cover the same nuclear and galactic sources with overlapping energy ranges. We will also use the *Swift* BAT spectrum above 20 keV, since this spectrum is consistent with the *NuSTAR* data and extends to higher energies.

All the components that are well constrained by the spectral fitting below 8 keV, including hot-gas emission and point-source power laws together with their cold absorbers, remain fixed in the fitting below. The remaining components correspond to scattered power law, Compton-scattered and transmitted AGN continuum. These are not well constrained by the low energy spectra and have large contributions to the *NuSTAR* band, so they are allowed to vary in the joint fit.

The normalization of the CGX1 power law is expected to vary from one epoch to another, so this parameter is different for the *XMM-Newton*, *Chandra*, and *NuSTAR* spectra. The normalization is fixed for the ACIS spectrum from which it was originally fit, the *difference* between *XMM-Newton* off-axis and *NuSTAR* on-axis is fixed as described in Section 5 and the difference between the *XMM-Newton* and ACIS observations is fit from the joint model. This component does not enter in the grating spectra. The joint nuclear and contamination models slightly overpredict the Fe lines in the *XMM-Newton* and *NuSTAR* spectra since the nuclear and contamination models account for some of these photons twice. Therefore, the narrow Gaussians introduced at 6.4 and 7 keV in Section 4.1 to solve this issue in the nuclear spectrum will only contribute to the HETG spectra and not to the other data sets.

For the Compton-scattered components, we use different models to account for the possible different geometries of the scattering material. Below, we describe the joint fits using either `pexmon` (Magdziarz & Zdziarski 1995), `MYTorus` (Yaqoob 2012) or `Torus` (Brightman & Nandra 2011) to reproduce the nuclear and galactic Compton-scattered components.

The nuclear spectrum is modeled as `phabs(`$N_{\rm H} = 10^{22}$`)` × `{lines+AGN}` and the contamination spectrum as `phabs`

Table 2
Parameters of the Best-fitting Models that use `pexmon` for the Compton Scattering Component

Joint fits: AGN components modeled with `pexmon`						
Component	Parameter	Model 1	Model 2	Model 3	Model 4	Model 5
Nuclear						
AGN	Γ	1.675 ± 0.004	1.82 ± 0.02	1.74 ± 0.01	2.5 ± 0.02	1.62 ± 0.03
continuum	E_c	1000.0	1000.0	1000.0	1000.0	24.1 ± 0.6
`pexmon`	Z	1.0	0.83 ± 0.05	1	2.08 ± 0.09	1
	$Z_{\rm Fe}$	1.0	1.73 ± 0.07	1	2.29 ± 0.07	1
	Incl.	$1.0^{+15.9}_{-1.0}$	$17.9^{+0.5}_{-6.5}$	$1.0^{+14.8}_{-1.0}$	$18.2^{+3.1}_{-5.5}$	$1.0^{+7.8}_{-1.0}$
	A_P	$1.86 \pm 0.024 \times 10^{-2}$	0.023 ± 0.001	$2.2 \pm 0.03 \times 10^{-2}$	0.140 ± 0.008	0.019 ± 0.001
`MYTorus`	$N_{\rm H}$	...	...	10 ± 10	3.82 ± 0.05	6.44 ± 0.06
	A_Z	0	0	0 ± 0.015	4.4 ± 0.5	10.6 ± 0.8
Scattered pl	A	$1.4 \pm 0.1 \times 10^{-4}$	$1.5 \pm 0.3 \times 10^{-4}$	$1.5 \pm 0.5 \times 10^{-4}$	$0 \pm 3.6 \times 10^{-5}$	$1.5 \pm 0.3 \times 10^{-4}$
Contamination						
`pexmon`	Z	1.0	6.28 ± 0.74	1	20 ± 2	1
	$Z_{\rm Fe}$	1.0	0.18 ± 0.06	1	0.12 ± 0.02	1
	Incl.	$1.0^{+19.0}_{-1.0}$	$1.0^{+18.0}_{-1.0}$	$1.0^{+18.1}_{-1.0}$	$18.1^{+3.2}_{-18.1}$	$1.0^{+12.4}_{-1.0}$
	A_P	$3.3 \pm 0.2 \times 10^{-3}$	$2.1 \pm 0.3 \times 10^{-2}$	$3.8 \pm 0.14 \times 10^{-3}$	0.215 ± 0.003	$3.4 \pm 0.2 \times 10^{-3}$
Scattered pl	A	$9.8 \pm 1.8 \times 10^{-5}$	$9.7 \pm 2.3 \times 10^{-5}$	$7.5 \pm 1.9 \times 10^{-5}$	$1.1 \pm 0.5 \times 10^{-4}$	$9.5 \pm 1.6 \times 10^{-5}$
$\chi^2_{\rm red}$		2.03	1.64	2.14	1.44	1.15

Notes. The photon index and cut-off energy are tied between the nuclear and contamination. The reflection fractions are fixed at -1. Units of $N_{\rm H}$ are 10^{24} cm^{-2}, angles are in degrees, and energies in keV. The normalizations of the `pexmon` components are denoted by A_P, of the transmitted nuclear component A_Z, and of the scattered power law A and are all in units of photons keV^{-1} s^{-1} cm^{-2} at 1 keV. The transmitted component is modeled with the zero-order component of `MYTorus` for an edge-on torus (inclination = 90 deg). The residuals to these models appear in Figure 11.

Table 3
Parameters of the Best-fitting Models that use `MYTorus` for the Compton Scattering Component

Joint fits: AGN components modeled with `MYTorus` and `Torus`							
Component	Parameter	Model 6	Model 7	Model 8	Model 9	Model 10	Model 11
Nuclear							
AGN	Γ	2.34 ± 0.02	2.31 ± 0.02	2.19 ± 0.02	2.40 ± 0.02	2.4 ± 0.03	2.31 ± 0.02
continuum	E_c	500	160	100	500	160	...
`MYTorus`/	$N_{\rm H}$	10.0 ± 1.8	10 ± 2.2	6.6 ± 0.9	7.1 ± 0.2	7.4 ± 0.2	8.9 ± 1.2
`Torus`	Incl.	76 ± 2.4	78.4 ± 1.4	75.8 ± 2.4	...	...	59.2 ± 2.3
	torus angle	...	...	...	...	...	34.9 ± 2.2
	A_Z/A_S	1.17 ± 0.36	1.54 ± 0.36	0.83 ± 0.26	0	0	0.66 ± 0.03
	A_{S90}	...	...	...	0.008 ± 0.8	0.19 ± 0.77	...
	A_{S00}	...	...	...	0.44 ± 0.01	0.43 ± 0.02	...
Scattered pl	A	$0 \pm 5 \times 10^{-5}$	$1.2 \pm 5.7 \times 10^{-5}$	$1.5 \pm 0.5 \times 10^{-4}$	$1.5 \pm 0.5 \times 10^{-4}$	$1.1 \pm 0.6 \times 10^{-4}$	$1.3 \pm 0.5 \times 10^{-4}$
Contamination							
`MYTorus`	$N_{\rm H}$	4.6 ± 0.2	5.0 ± 0.2	7.0 ± 5.6	7.1	7.4	3.9 ± 0.5
	Incl. (deg)	85.1 ± 0.4	84.7 ± 0.8	80.0 ± 6.3	...	...	79.1 ± 1.6
	A_S	0.95 ± 0.14	0.81 ± 0.17	0.26 ± 0.36	...	...	0.24 ± 0.07
	A_{S90}	...	...	...	2.12 ± 0.7	2.35 ± 0.74	...
	A_{S00}	...	...	...	0.036 ± 0.012	0.03 ± 0.74	...
Scattered pl	A	$2.3 \pm 0.4 \times 10^{-4}$	$2.2 \pm 0.4 \times 10^{-4}$	$1.8 \pm 0.4 \times 10^{-4}$	$2.6 \pm 0.5 \times 10^{-4}$	$2.6 \pm 0.5 \times 10^{-4}$	$2.0 \pm 0.4 \times 10^{-4}$
$\chi^2_{\rm red}$		1.195	1.11	1.12	1.106	1.06	1.125

Notes. The photon index and cut-off/termination energy are tied between the nuclear and contamination spectra. Units of $N_{\rm H}$ are $\times 10^{24}$ cm^{-2}. The normalizations of the `MYTorus` Compton-scattered components are denoted by A_S in the traditional implementation, and A_{S90}, A_{S00} for the forward scattering and back reflection components in the decoupled implementation. The normalizations of the transmitted nuclear component and the scattered power law are A_Z and A, respectively. In the default configuration models quoted here, A_Z and A_S were tied. Untying these normalizations resulted in vanishing A_Z. All normalizations are in units of photons keV^{-1} s^{-1} cm^{-2} at 1 keV, angles are in degrees and energies in keV. The residuals to these models appear in Figure 13.

($N_{\rm H} = 1.16 \times 10^{22}$) × {`apec +phabs(`$N_{\rm H} = 2.2 \times 10^{22}$`) [mekal+mekal+gsmooth(0.065 keV) × Mekal]+lines+ AGN`}. The AGN components include scattered and Compton-scattered power laws, fluorescent line emission and, in the nuclear spectrum only, a transmitted continuum—the parameters of these are summarized in Table 2 for the `pexmon` Compton scattering models and in Table 3 for the `MYTorus`/`Torus` Compton scattering models. The rest of the parameters were fitted in the previous sections and frozen in the joint fits. These are the emission line parameters, summarized in

Table 4
Emission Lines Fitted to the Nuclear Spectrum, the First 15 from Sambruna et al. (2001), where Line Energies were Allowed to Vary within the Uncertainties Quoted Therein

Emission lines in the nuclear and contamination spectra				
Energy (keV)	sigma (keV)	Norm. Nuclear	Norm. Cont.	ID
2.005	1.7×10^{-3}	1.08×10^{-5}	1.02×10^{-5}	Si XIV
2.308	4.7×10^{-3}	7.12×10^{-6}	4.35×10^{-6}	S II–X
2.377	3.7×10^{-3}	5.95×10^{-6}	2.45×10^{-6}	Si XIV+ S XII
2.400	7.9×10^{-3}	1.97×10^{-6}	9.96×10^{-7}	S XIV
2.435	9.3×10^{-3}	9.57×10^{-6}	...	S XV
2.46	2.1×10^{-3}	8.31×10^{-6}	7.07×10^{-6}	S XV
2.62	1.4×10^{-3}	4.88×10^{-6}	7.40×10^{-6}	S XVI
2.88	2.9×10^{-3}	2.17×10^{-6}	1.85×10^{-6}	S XV
2.96	5.7×10^{-3}	3.30×10^{-6}	6.18×10^{-7}	Ar II–XI
3.27	1.2×10^{-3}	...	2.6×10^{-6}	Ar XVIII
3.90	4.8×10^{-3}	5.30×10^{-7}	1.07×10^{-6}	Ar XVIII
3.69	1.0×10^{-3}	3.00×10^{-6}	...	Ca II–XIV + Ar XVII
3.686	1.0×10^{-3}	2.65×10^{-6}	5.42×10^{-7}	Ca II–XIV + Ar XVII
6.66	1.0×10^{-2}	9.97×10^{-6}	...	Fe XXV
6.95	1.0×10^{-2}	7.30×10^{-6}	...	Fe II–XVII
2.18	1.5×10^{-6}	3.00×10^{-6}	3.69×10^{-6}	Si XIII Kβ
3.11	5.8×10^{-3}	2.90×10^{-6}	2.04×10^{-6}	S XVI Kβ
5.41	1.0×10^{-4}	3.70×10^{-6}	1.58×10^{-6}	Cr I
5.88	1.0×10^{-3}	3.11×10^{-6}	4.76×10^{-7}	Cr XXIV
6.50	5.0×10^{-2}	3.30×10^{-5}	7.81×10^{-6}	Fe XXV triplet
7.47	1.0×10^{-3}	1.36×10^{-5}	...	Ni I

Notes. Line widths were fitted to the nuclear spectrum and frozen to those values in the fit to the contamination spectra. Unless otherwise specified, lines correspond to Kα transitions. Lines with vanishing normalizations were eliminated. All these parameters were frozen in the joint fits described in Section 6.

Table 5
Continuum Components in the Contamination Spectrum, Corresponding to Hot Diffuse Gas, a SN Remnant and the Power Law Spectrum of CGX1, and other X-ray Binaries Together

Continuum components in the contamination spectrum					
Model	kT	Z	z	Γ	Norm.
`APEC`	0.238	1.0	1.45×10^{-3}	...	8.66×10^{-3}
`Mekal`	0.09	0.5	7.80×10^{-2}	...	2.37
`Mekal`	1.09	7.5	-6.58×10^{-3}	...	1.98×10^{-4}
`Mekal`	9.15	7.5	-2.86×10^{-3}	...	6.33×10^{-4}
power law	...	...	...	1.80	4.27×10^{-4}

Note. All these parameters were frozen in the joint fits described in Section 6.

Table 4, and the thermal emission components summarized in Table 5.

6.1. Compton Scattering Modeled with `pexmon`

The following analysis uses the `pexmon` model to represent the Compton-scattered components. This model assumes that the scattering structure has a slab geometry and infinite optical depth. A directly transmitted AGN component is also allowed in the fit to the nuclear spectrum and is modeled using the zero-order `MYTorus` model, which is more accurate than a simple absorbed power law model in the Compton thick regime. The Ni edge is not included in `pexmon` so we introduced it with the model `zedge` at the systemic redshift of Circinus. The depth of this feature with $\tau = 0.1$ was fixed based on the measured Ni Kα flux.

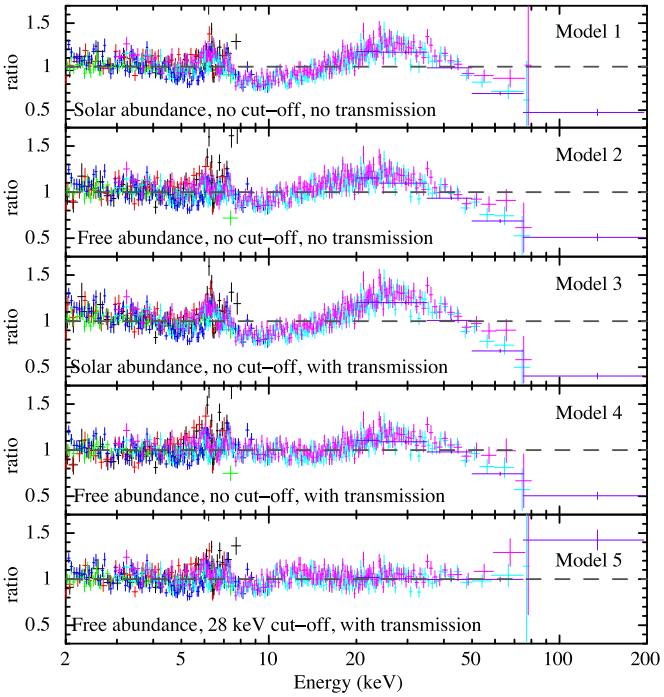

Figure 11. Residuals of all the data sets to the models using `pexmon` for the Compton-scattered components, as described in Section 6.1. The HEG (black) and MEG (red) nuclear data are only fit with the nuclear model, the ACIS spectrum (green) is only fit with the contamination model, and the *XMM-Newton* (blue), *NuSTAR* A and B (magenta, cyan), and *Swift* BAT (purple) spectra are fit with the sum of both components. The only configuration capable of reproducing the high energy curvature involves a strong transmitted power law, shown in the bottom panel. This model is plotted in Figure 12.

(A color version of this figure is available in the online journal.)

To begin, we assume that the nuclear obscurer has the same optical depth as the scatterer so that no transmitted flux reaches the observer and therefore the zero-order `MYTorus` model normalization is fixed at zero. This is the reflection-dominated case. The variable `pexmon` parameters are the intrinsic AGN power-law slope Γ, the inclination angle of the scattering slab, and the normalization of this component. The reflection fraction is fixed to -1, i.e., only reflected emission is considered and the reflector is assumed to cover half the sky of the primary source. The same model setup is used for the nuclear and galactic Compton scatterers. The parameters of the nuclear and galactic Compton scatterers vary independently except for the power-law slope Γ, which is free to vary but tied between both these components and the scattered power laws.

We allow only Γ, the inclination angle, and normalization of both `pexmon` scatterers and the normalization of both scattered power-law components to vary, and keep the abundances fixed at the solar value and the cut-off energy fixed at 1000 keV. This approach gives a $\chi^2_{\rm red} = 2.03$ for 2639 dof and the residuals show a clear peak at 30–40 keV. This model is not able to reproduce the curvature of the high-energy spectrum, and its residuals are shown in the top panel in Figure 11 (model 1).

Allowing the abundance and Fe abundance of both Compton scatterers to vary produces a better fit with $\chi^2_{\rm red} = 1.64$ for 2635 dof. The spectral bump at 30–40 keV is better reproduced although still apparent in the residuals, as shown in the second panel in Figure 11 (model 2). The fitted overall and Fe abundances for the nuclear Compton scatterer are

$Z = 0.83 \pm 0.05\ Z_{\odot}$ and $Z_{\rm Fe} = 1.73 \pm 0.07\ Z_{\odot,{\rm Fe}}$, respectively, while for the contamination component they are $Z = 6.29 \pm 0.75\ Z_{\odot}$ and $Z_{\rm Fe} = 0.18 \pm 0.06\ Z_{\odot,{\rm Fe}}$. This combination of sub- and super-solar abundances makes the Compton scattering peaks appear at different energies, below 20 keV for the nuclear component and above 20 keV for the contamination, producing an overall broader Compton hump. This fit, however, is still unsatisfactory.

Keeping the abundances fixed at solar and freeing the cut-off energy of the intrinsic power law also gives a poor fit with $\chi^2_{\rm red} = 1.91$ for 2638 dof. In this case, the cut-off energy is tied between the nuclear and galactic Compton scatterers, so both components have similar shapes and cannot mimic a broader Compton hump. The best-fitting folding energy is 292 ± 26 keV and the AGN continuum photon index is $\Gamma = 1.60 \pm 0.02$.

As an alternative, we incorporated a transmitted AGN component in the nuclear spectrum with variable column density and normalization and repeated the procedure above with these additional free parameters. We model this component as the transmitted spectrum through an edge-on torus using the zero-order component of `MYTorus` with its inclination fixed at 90 deg. As above, we begin with `pexmon` models with fixed cut-off energies well above the observed range, abundances fixed to solar values and free inclination angles. The normalizations of all scattered power laws, Compton-scattered components, and the transmitted spectrum are allowed to vary freely. The fit is poor, with a $\chi^2_{\rm red} = 2.14$ for 2637 dof. The transmitted component normalization vanishes and therefore its $N_{\rm H}$ is unconstrained. The same feature as in models 1 and 2 appears in the residuals, shown in the third panel in Figure 11 (model 3). Allowing the overall and Fe abundances of both Compton scattering components to vary improves the fit as in the reflection-dominated cases, to $\chi^2_{\rm red} = 1.44$ for 2633 dof. Although this fit is significantly better, it still produces a broad peak at 30 keV in the residuals, shown in the fourth panel in Figure 11 (model 4).

We again return to solar abundances and assume a cut-off power law for the intrinsic AGN component, tying the folding energy in `pexmon` to E_c of the cut-off power law that is multiplied by the zero-order `MYTorus` component. This setup gives a much better fit with $\chi^2_{\rm red} = 1.15$ for 2636 dof. This model reproduces well the curvature of the *NuSTAR* spectra, although it underpredicts the higher energy bins covered by *Swift* BAT. The cut-off energy is fitted at 24.1 ± 0.8 keV, the nuclear $N_{\rm H} = (6.44 \pm 0.06) \times 10^{24}$ cm^{-2}, and the photon index of the AGN power law and all its scattered components is $\Gamma = 1.62 \pm 0.03$, the inclination angles of both `pexmon` models converged to 0. The normalization of the nuclear (unabsorbed) power law is 10.6 ± 0.8 photons keV^{-1} s^{-1} cm^{-2} at 1 keV while that of the nuclear `pexmon` model is 0.019 ± 0.001 in the same units. In this model, the transmitted power-law component dominates the total spectrum above 20 keV. The (unabsorbed) 2–10 keV flux of the nuclear power law is 3.9×10^{-8} erg s^{-1} cm^{-2}. The residuals to this model are shown in the last panel in Figure 11 (model 5) and the model itself is shown in Figure 12. In this model, the transmitted power dominates the total spectrum above 15–20 keV and produces 93% of the energy in the 30–79 keV band. The best-fitting parameters to the models shown in Figure 11 are summarized in Table 2.

In summary, modeling the Compton-scattered components with `pexmon` only produces a good fit when the transmitted power law is included and the intrinsic AGN power law has a cut-off within the observed energy range. In this scenario, the optical depth of the obscurer and scatterer are necessarily different since `pexmon` only allows an infinite optical depth. The cut-off energy is surprisingly low, at 28 keV, and this underpredicts the highest energy bins. In this model, the AGN power-law photons that have traversed the obscurer unscattered dominate the total (nuclear+contamination) spectrum above 20 keV. In the majority of these fits, including the best-fitting, transmission-dominated model, the AGN power law was flat with a photon index $\Gamma < 1.8$.

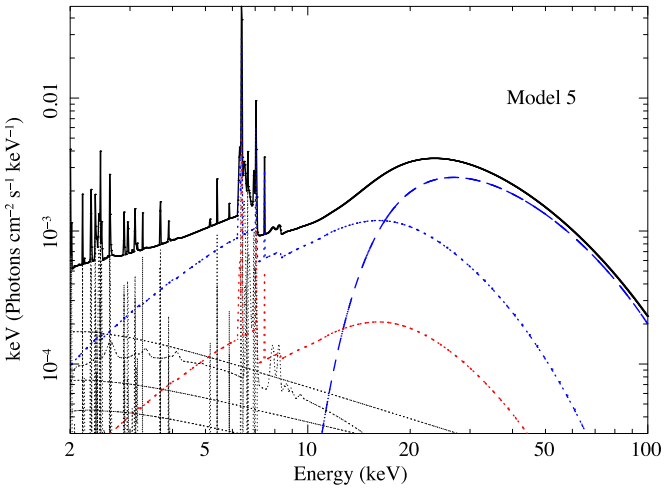

Figure 12. Best-fitting model of the model group using `pexmon` for the Compton-scattered components. The dashed blue line represents the transmitted power law component (i.e., the nuclear photons that travel through the absorber unscattered). The dotted lines represent the nuclear (blue) and contamination (red) Compton-scattered components. In this model, the transmitted power dominates the total spectrum above 15–20 keV and produces 93% of the energy in the 30–79 keV band.

(A color version of this figure is available in the online journal.)

6.2. *Compton Scattering Modeled with* `MYTorus`

We expect that the Compton-scattered component should be modeled better with a torus model that takes into account the toroidal geometry of the scatterer, modeling the transmitted and Compton-scattered components consistently. We thus replace the `pexmon` model with the `MYTorus` Compton-scattered component.

We consider first a uniform torus, so that the transmitted and scattered `MYTorus` components will have the same column densities and inclination angles and are illuminated by the same power-law continuum. As in the previous section, we also tie the photon index of the scattered and Compton-scattered components in the nuclear and contamination spectra. As a first step, we consider an incident power law with no cut-off in the observable range and solar metallicities. The Ni edge is not included in the `MYTorus` scattered component so we again introduced it with the model `zedge` at the systemic redshift.

Allowing the photon index of the AGN continuum to vary, along with the inclination angle, $N_{\rm H}$ and normalization of both Compton scatterers, and the normalization of the scattered power laws produced a fit with $\chi^2_{\rm red} = 1.195$ for 2637 dof. This quality is similar to the best `pexmon` model described above, the residuals are shown in the top panel in Figure 13 (model 6). Note, however, that the current setup is slightly more restrictive in the sense that the transmitted and Compton-scattered components are forced to have the same normalization and obscuration parameters, we allow no cut-off in the power law and the metallicity is fixed at the solar value. nuclear=10.

We now relax the assumption that the nuclear obscurer and scatterer are identical by allowing the $N_{\rm H}$ of the nuclear

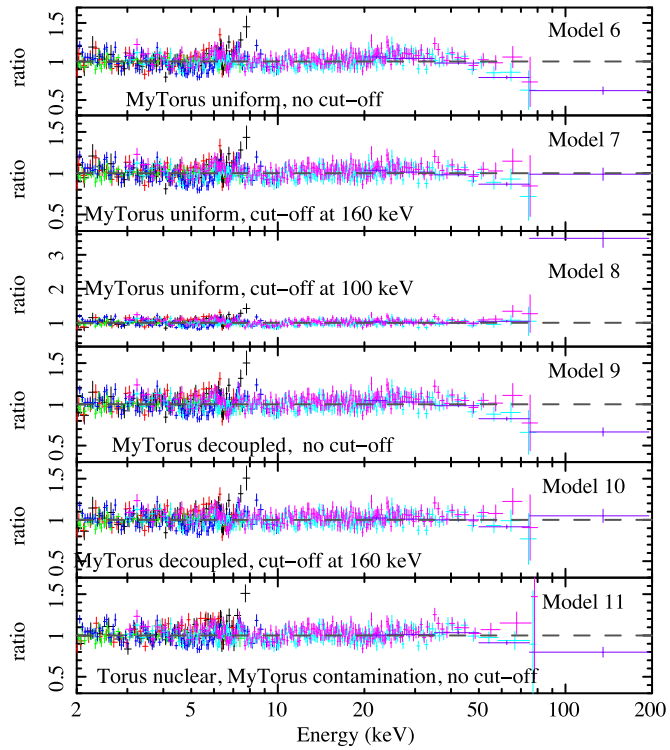

Figure 13. Residuals of all the data sets to the models using `MYTorus` for the Compton-scattered components, as described in the text. The last panel uses `Torus` instead of `MYTorus` for the nuclear transmitted and Compton-scattered components together. These models reproduce well the curvature around 30 keV using solar metallicities and little or no transmitted components, consistent with the parameters of the scatterer. A cut-off in the power law is required above the *NuSTAR* spectral range to reproduce the *Swift* BAT data points. Note that the cut-off energies refer to a termination energy and not an exponential roll-over of the power law flux. The models corresponding to panels 2, 5, and 6 are shown in Figure 14. Colors are as described in Figure 11.

(A color version of this figure is available in the online journal.)

transmitted and Compton-scattered components to be different. This could be the case in a patchy torus, where the line-of-sight $N_{\rm H}$, i.e., in the transmitted component, differs from the global average $N_{\rm H}$ which shapes the scattered component. This results in only a small improvement in the quality of the fit, $\chi^2_{\rm red} = 1.182$ for 2636 dof and the residuals show the model still overpredicts the data above 80 keV, while the Compton hump around 30–40 keV is well reproduced.

Returning to the uniform torus model but allowing the normalization of the transmitted power law to vary freely with respect to the nuclear Compton scatterer represents a uniform torus with a variable covering fraction. This setup produces a similar fit to the first case, $\chi^2_{\rm red} = 1.187$ for 2636 dof. In this fit the normalization of the transmitted power law drops to zero and reduces somewhat the $N_{\rm H}$ of the nuclear scattered component from 10^{25} to $(8 \pm 0.9) \times 10^{24}$ cm^{-2}. The most notable residuals are, as in all cases in this subsection, an overprediction of flux at high energies.

To deal with the high-energy slope we wish to introduce a cut-off to the AGN power law. `MYTorus`, however, does not allow a cut-off energy as a free parameter in the Compton-scattered component but instead provides several tables calculated for different 'termination energies'. We replaced the power law multiplying the zero-order `MYTorus` component by a cut-off power law and fixed its cut-off energy to that of the termination energy of the Compton-scattered table used for each fit. The termination energy implies an abrupt drop in the flux rather than the typical exponential rollover implied by a cut-off. Therefore, the termination energy does not represent a cut-off energy in the usual sense and can only be loosely interpreted as an upper limit of where the rollover cut-off should be. The difference in spectral shapes in the scattered components begins close to the termination energy and, as all termination energies we will use are at or above 100 keV, where the spectral resolution is poor the precise spectral shape has little impact on the fit. The main feature we explore is whether the flux at the highest *Swift* BAT energy bins is over- or under-predicted by each model. Using a cut-off/termination energy of 160 keV results in a $\chi^2_{\rm red} = 1.11$ for 2637 dof with the corresponding residuals shown in the second panel in Figure 13 (model 7). To demonstrate that 160 keV gives the best results, we refit the model using 100 keV and 200 keV cut-offs/termination energies. Lowering to 100 keV produces a worse fit, $\chi^2_{\rm red} = 1.22$ for 2367 dof, where the highest energy bins are under-predicted, as shown in the third panel in Figure 13 (model 8). Increasing the energy to 200 keV also produces a slightly worse fit than $E_{\rm c} = 160$ keV, with $\chi^2_{\rm red} = 1.13$ for 2637 dof.

Using the best-fitting model, with a cutoff/termination energy at 160 keV, we explore the patchy torus possibility by untying the $N_{\rm H}$ of the nuclear Compton scatterer from that of the transmitted component. The fit is not much better, with $\chi^2_{\rm red} = 1.108$, and both values of $N_{\rm H}$ remain consistent with 10^{25} cm^{-2}. Returning to the uniform torus, but allowing for different covering fractions of the nuclear scatterer by untying the normalizations of the transmitted and nuclear Compton-scattered components, produces $\chi^2_{\rm red} = 1.108$ with a vanishing transmitted component.

6.2.1. *Decoupled* `MYTorus` *Implementation*

We also allow for a patchy torus where some reflection off the front of background clouds bypasses the clouds toward the line of sight, as suggested in Yaqoob (2012). This scenario is implemented in `MYTorus` by using two Compton scatterers, one edge-on and one face-on, where the corresponding normalizations, A_{90} and A_{00}, vary independently. Each Compton scatterer has its associated Fe Kα and Kβ lines. We use this setup for the Compton-scattered components of the nuclear and the contamination spectra. At first, we tie together the $N_{\rm H}$ of all four Compton-scattered components. Allowing all the Compton-scattered, scattered, and transmitted power-law normalizations to vary independently produces a good fit with $\chi^2_{\rm red} = 1.106$ for 2367 dof and a vanishing transmitted component. The residuals of this model are shown in the fourth panel in Figure 13 (model 9).

Untying $N_{\rm H}$ for the nuclear and contamination spectra produces $\chi^2_{\rm red} = 1.102$ for 2366 dof, a vanishing nuclear A_{90} and small contamination A_{00}. It does not make sense to decouple the $N_{\rm H}$ of the forward scattering and back reflection components of the nuclear component since they refer to the same distribution of clouds; the same reasoning applies to the Compton-scattered components in the contamination model. It can happen, however, that the line-of-sight $N_{\rm H}$ is different from the global average. Allowing $N_{\rm H}$ to vary independently for the transmitted and for the Compton scatterers in the nucleus does not produce a better fit and, in this case, the transmitted component normalization also vanishes.

All of these fits reproduce well the curvature of the nuclear spectrum but overpredict the highest energy *Swift* BAT spectral bins as in the case of coupled `MYTorus` models. To solve this issue, we repeat our procedure with the cut-off power laws

and termination energies. With a cut-off/termination energy of 160 keV, we obtain a $\chi^2_{\rm red} = 1.056$ for 2637 dof. These residuals are shown in the fifth panel in Figure 13 (model 10) and the model is shown in the middle panel in Figure 14. Fitting the nuclear and contamination $N_{\rm H}$ values separately does not improve the fit.

6.3. Compton Scattering Modeled with `Torus`

As the geometry of the torus is not known, we also tested the applicability of the `Torus` model (Brightman & Nandra 2011), which assumes a spherical obscurer with conical polar openings of a variable opening angle, instead of the toroidal structure with fixed opening angle used in `MYTorus`. This model combines the Compton scattered and transmitted components, which are therefore always modeled consistently. It is not possible within this model to separate the photons that went through the torus unscattered from those that suffered one or more scatterings, such that a fraction of the `Torus` flux will correspond to transmitted photons. For the high column densities measured, however, this transmitted flux is always a small fraction of the Compton scattered flux. `Torus` cannot be used to model the Compton scattering of the contamination spectrum since this spectrum is necessarily out of the line of sight to the AGN and therefore does not contain a transmitted component.

We model the Compton scattering in the contamination spectrum first with `pexmon` and then with `MYTorus`. `Torus` self-consistently predicts the Kα emission lines of all the relevant elements, so we removed Gaussian lines at 2.96, 3.69, 5.41, and 7.47 keV, corresponding to the Kα transition of Ar, Ca, Cr, and Ni, from the nuclear model to avoid double counting them. Keeping all the AGN-related photon indices tied, a free torus opening angle, free inclination, and free normalizations of the scattered power laws and contamination Compton scattering component produces a $\chi^2_{\rm red} = 1.24$ for 2636 dof. We now replace `pexmon` in the contamination model with `MYTorus`. Repeating the fit above, with free $N_{\rm H}$ and inclination angle values for the `MYTorus` Compton-scattered component produces a better fit with $\chi^2_{\rm red} = 1.125$ for 2636 dof. The residuals to this model are shown in the bottom panel in Figure 13 (model 11) and the model is shown in the bottom panel in Figure 14. This model produces a better fit than `MYTorus` in the default configuration when no cut-off is allowed below 500 keV in the incident power law, and it only overestimates the highest energy BAT points by tens of percent. We contend that a cut-off at similar energies as the `MYTorus` case would improve this fit further but it is not possible to introduce this feature with the current implementation.

In summary, the use of either `Torus` or `MYTorus` produces a better description of the spectra than `pexmon` when we consider reflection-dominated models. As mentioned in the previous subsections, `pexmon` can produce an acceptable fit when a strong transmitted component is incorporated. In all the fits with `Torus` and `MYTorus` the transmitted component is negligible in the observed energy band, the column densities of the nuclear absorber range from (8–10) $\times 10^{24}$ cm^{-2} and the AGN photon index is in the range $\Gamma = 2.2$–2.4. Using cut-off/termination energies above 100 keV and solar metallicities, which are inherent in the models, prove adequate. Different geometries of the obscurer/scatterer produce similar quality fits so it is not possible to discriminate between a patchy or homogeneous torus or between a toroidal or spherical structure. The best-fitting parameters of the models used in Figure 13 are summarized in Table 3. We note that the `MYTorus` tables are only calculated for column densities up to $N_{\rm H} = 10^{25}$ cm^{-2} implying that some of

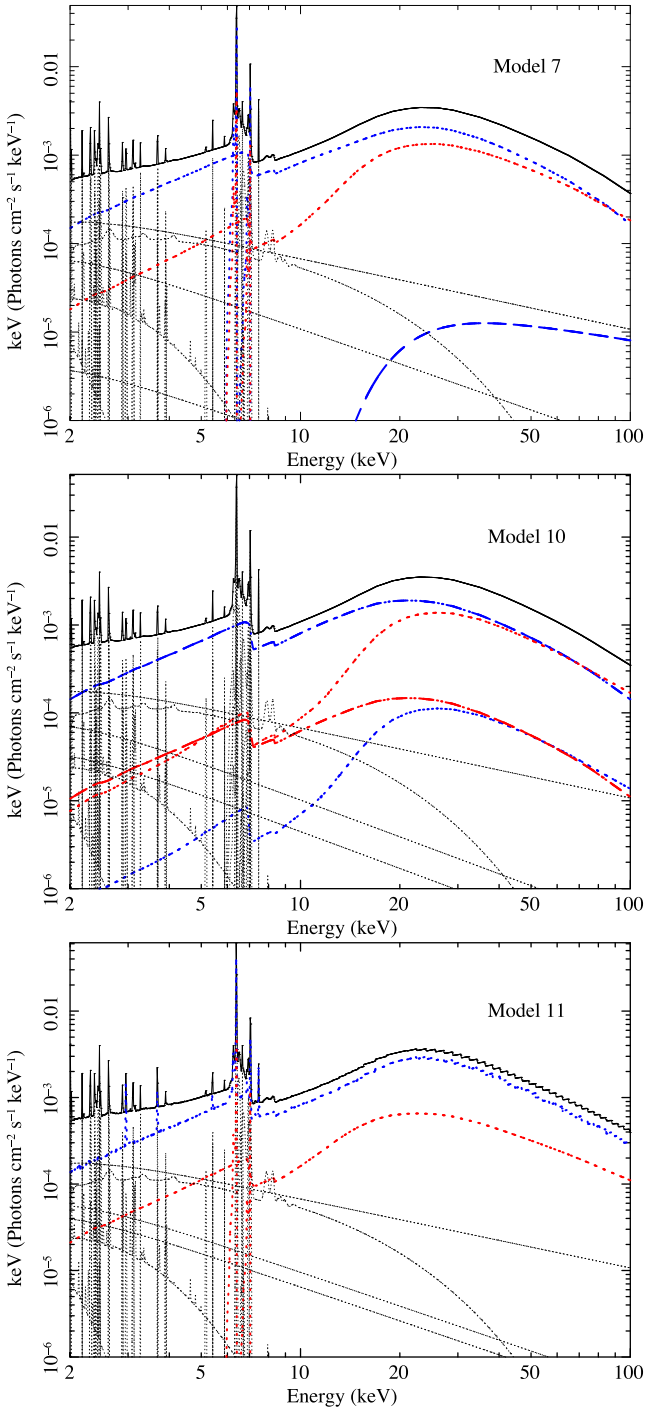

Figure 14. Best-fitting models of the model group using `MYTorus` and `Torus` for the Compton-scattered components. Blue lines represent nuclear components and red lines contamination components. Top panel: uniform torus modeled with coupled `MYTorus` transmitted (dashed lines) and Compton-scattered (dotted lines) components. The contamination Compton scatterer in red dashed lines becomes comparable to the nucleus at high energies. The transmitted component is negligible. Middle panel: Decoupled `MYTorus` component having forward scattered (dotted lines) and reflected (dot-dashed lines) in both nuclear and contamination spectra. As above, the nuclear and contamination scatterer components become comparable at about 30 keV and the transmitted component is negligible. Bottom panel: similar to the top panel but using `Torus` instead of `MYTorus` for the nuclear Compton-scattered plus transmitted spectra. Given the fitted torus parameters, the transmitted component (incorporated in the blue dashed line) should be a small fraction of the nuclear spectrum. The residuals of the spectra to these three models are shown in Figure 13 in panels 2, 5, and 6. The models are discussed in Sections 6.2 and 6.3.

(A color version of this figure is available in the online journal.)

the 1σ error ranges for this parameter in Table 3 saturate at the maximum available value and a significant upper limit cannot be obtained. The `Torusmodel`, however, is calculated for column densities up to $N_{\rm H} = 10^{26}$ cm^{-2}, and has a best-fitting value of 8.9 ± 1.2 such that it is completely constrained within the available range.

7. TIMING CONSTRAINTS ON THE HIGH-ENERGY SPECTRUM

One way to differentiate between a transmission-dominated scenario, as preferred by the `pexmon` modeling, and a Compton-scattering-dominated scenario, as preferred by the `MYTorus` and `Torus` models, is by their temporal behavior. In particular, we note that the direct AGN X-ray continuum is highly variable, as has been observed in large samples of unobscured sources. If these AGNs are intrinsically the same as obscured sources, then the primary continuum should be equally variable in obscured AGNs. Therefore, at high energies where the continuum might "punch" through the obscuring material, obscured sources should be as variable as unobscured ones. One example is the obscured AGN NGC 4945, where the lower obscuration toward the nucleus allows a variable power law to be seen at high energies, as suggested by Iwasawa et al. (1993) using *Ginga* data and studied in detail with *NuSTAR* (Puccetti et al. 2014).

We constructed power spectra of the high-energy *NuSTAR* light curves to compare with the expected power spectrum of a transmitted component. We used XSELECT to extract 30–79 keV photons for the source region and for a background region of equal area on the same detector. Light curves were then constructed by binning the photons in 100 s equally spaced bins of which only those with exposure ratios over 90% were retained. The low orbit of *NuSTAR* produces 2 ks gaps in the lightcurves every 6 ks cycle. The first observation produces light curves covering 90 ks, while the second observation is split into three segments of 30–80 ks duration separated by two gaps of 60 and 100 ks. We computed separate power spectra for each module and for the on-axis and off-axis observations using the Mexican-hat filtering method described in Arévalo et al. (2012). This method can easily combine the different segments of the second observation and is largely unaffected by gaps in the light curves. In this normalization, the variability power equals the variance of the filtered light curve divided by the average count-rate squared.

The observational Poisson noise in the light curves contributes variability power with a white noise (flat) spectrum. In Figure 15, we plot power×frequency so this flat spectrum appears as a linear rising trend. The normalization of the expected Poisson noise spectrum for each light curve was calculated from the source and background counts in each time bin and the resulting spectra are plotted as dashed lines. The on-axis observation produced slightly smaller errors and therefore lower Poisson noise than the off-axis observation.

The power spectrum of AGN continuum emission has been measured for many type 1 Seyfert galaxies, where the 2–10 keV range is largely unobscured. The power spectra typically have a broken power-law shape, where the low- and high-frequency slopes are -1 and -2, respectively (e.g., Markowitz et al. 2003; McHardy et al. 2004, 2005, 2006; Markowitz et al. 2007). The normalization below the break frequency is very similar among different AGN. When the power spectra are normalized by the average count rate squared, the dimensionless quantity power × frequency is typically in the range 0.01–0.1. The distinguishing feature of the power spectra of different AGNs is the position of

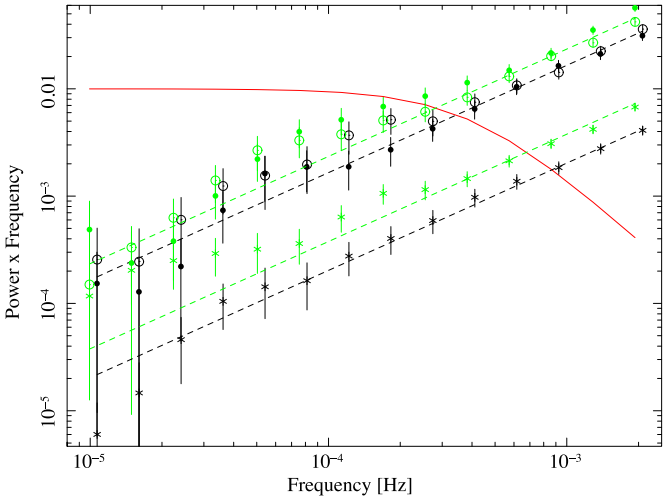

Figure 15. Power spectra of the high energy (30–79 keV) *NuSTAR* light curves. The on-axis observations are plotted in black and off-axis in green, while filled circles represent FPMA source light curves and open symbols represent FPMB source light curves. The power spectra of the background regions only are plotted in stars following the same color convention. The dashed lines show the power spectra expected for Poisson noise only for each case. The solid red line represents the power spectrum of the direct continuum for an AGN of the same mass and accretion rate as Circinus. The high-energy light curves are consistent with simple Poisson noise and their variability is far below the expected value for a transmitted AGN continuum.

(A color version of this figure is available in the online journal.)

the break timescale, which depends on the black-hole mass and accretion rate. McHardy et al. (2006) fit the relation

$$\log T_B = 2.1 \log M - 0.98 \log L_{\rm bol} - 2.28, \qquad (1)$$

where T_B is the break timescale in days, M is the black hole mass in units of $10^6\ M_\odot$ and $L_{\rm bol}$ is the bolometric luminosity in units of 10^{44} erg s^{-1}. Assuming $M = 1.5$ and $L_{\rm bol} = 0.4$ for Circinus, the break timescale is expected at 0.03 days and the corresponding break frequency is 4×10^{-4} Hz. A bending power law model with low-frequency normalization of 0.01 and this break frequency is plotted as a solid red line in Figure 15. If the high-energy emission we observed in Circinus were mostly a transmitted power law component, we would expect its power spectrum to resemble this curve.

The measured power spectra closely follow the Poisson noise level and are far below the intrinsic variability spectrum expected from a transmitted component. Note that symbols of equal color correspond to simultaneous observations so the difference between their filled and open circles are due to differences in the Poisson noise, background contribution, or other systematic effects. For comparison, we also plot the background power spectra for module B of each observation, where no intrinsic variability is expected. The off-axis background spectrum deviates most strongly from the Poisson spectrum at low frequencies. This additional variability in the background can contribute to the source spectrum as well, so similar amplitude deviations can be attributed to unaccounted variations in the background count rate. Figure 16 shows the observed *NuSTAR* lightcurves combining FPMA and B data in black markers and the average count rate for each observation in blue solid lines. The error bars represent the Poisson noise expected in these background-subtracted bins. For a visual comparison of the variability we would expect to see in the power law component, we overplotted a random realization of a light curve whose underlying power spectrum follows the red model in Figure 15.

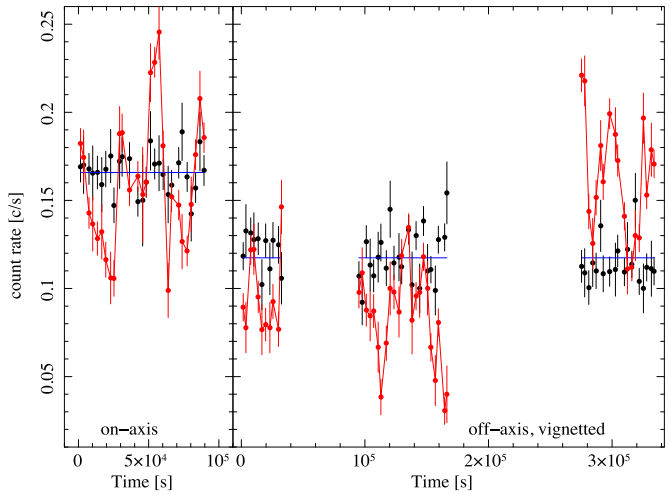

Figure 16. Circinus *NuSTAR* light curves in 30–79 keV band, A and B module data combined, binned in 3 ks, in black markers with error bars. The horizontal solid blue lines represent the average count rate for each observation; the fit to this model produces $\chi^2/\mathrm{dof} = 20/28$ for the on-axis observation (left) and 68/53 for the off-axis observations (right). The red markers and lines are a random realization of a light curve whose underlying power spectrum corresponds to the red line in Figure 15, i.e., the expected amplitude and timescales of variability for the intrinsic power-law emission for an AGN of the same mass and accretion rate as Circinus. The difference in average count rate between both observations is caused by vignetting; their calibrated fluxes are the same.

(A color version of this figure is available in the online journal.)

The simulated light curve was sampled to match the observed 100 s binned *NuSTAR* light curve, scaled to the average count rate, and Poisson noise was added at the appropriate level. This simulated lightcurve was then binned in 3 ks bins, in the same way as the real light curves and is plotted in red markers and lines in Figure 16.

The minimal variability observed in the light curves is largely consistent with a constant flux affected by Poisson noise. This is the expected behavior if the high-energy flux indeed arises from Compton-scattered emission over large distances, i.e., across the torus, and not to a transmitted power-law component. We note, however, that the power spectra are normalized by the square of the average count rate. If the 30–79 keV flux contained both a variable transmitted component and a constant Compton-scattered component, then the normalized variance of the transmitted component would be reduced by the contribution of the Compton-scattered flux to the normalization. The difference of about a factor of 10 between the upper limit on the measured power at low frequencies and the expected power spectrum limits the maximum contribution of the transmitted flux to about a third of the total flux in this band. Therefore, under the assumption that the intrinsic X-ray continuum of obscured and unobscured AGNs behave in the same way, the spectral decomposition where the transmitted component contributes to 90% of the flux in this band, such as the last `pexmon` model described, can be ruled out.

We explored longer-term variability in the hard X-ray band using the *Swift* BAT 70 month data taken between 2004 and 2010. We found that the full 14–100 keV band light curve of a region centered on Circinus, binned in one-month intervals, shows significant variability, but note that the telescope PSF of 17′ allows for significant contamination of nearby sources. Splitting the data into several energy bands shows that the variability is only present in the softest BAT band. We constructed light curves in five energy bands, 14–20, 20–24, 24–35, 35–50, 50–75, and 75–100 keV, binned in 10^7 s bins to produce uniform S/N light curve points. Each light curve contains 18 points. Fitting a constant value to each light curve produced $\chi^2_{\mathrm{red}} = 5.21$ for the first band and values between 0.67 and 1.51 for all other bands. This constant flux null-hypothesis can be rejected with high significance only for the 14–20 keV band, with a fractional rms = 32%. In all other bands, the significance of the variability is less than 95%. Section 5 shows that the nuclear flux within 11″ up to 10 keV has not changed between two observations taken 12 yr apart, so that the 14–20 keV variability detected by BAT probably corresponds to variations in contaminating sources within its field of view. The BAT extraction region includes the entire Circinus galaxy, the bright and variable CGX1 and ULX5, as well as other potential sources in their vicinity. These XRBs, however, have softer spectra than the nucleus, and at high energies, above 20 keV, their contribution is negligible. We note that although the angular resolution of *NuSTAR* cannot separate the nucleus from CGX1, our *NuSTAR* extraction is not contaminated by ULX5 or other sources further away, which do pose a problem to all other hard X-ray observatories.

Combining the *Swift* BAT light curves above 20 keV to improve the S/N and fitting to a constant results in $\chi^2_{\mathrm{red}} = 1.48$, which rejects the hypothesis of constant flux with less than 90% significance and has a fractional rms of only 7.7%. The count rate in the 20–100 keV light curve is over three times higher than in the variable 14–20 keV, so the lack of significant variability is not due to larger uncertainties on the light curve bins. We conclude that the long-term behavior of the high-energy nuclear flux is consistent with a constant value over the 70 months probed by BAT. The lack of high-energy variability in the BAT light curves is consistent with the Compton-scattered-dominated spectrum, since a variable transmitted power law would be more dominant at higher, not lower, energies. Therefore, if the 14–20 keV variability originated in the nuclear power law, the higher energy bands would be even more variable.

The variability analysis rules out the scenario where the AGN continuum "punches" through the obscurer in order to dominate the spectrum above 30 keV. The pure Compton scattering scenario is therefore preferred.

8. DISCUSSION AND CONCLUSIONS

We presented the X-ray spectra of Circinus using a combination of *NuSTAR*, *Chandra*, *XMM-Newton*, and *Swift* data.

The high angular resolution *Chandra* data were used to separate the nuclear (central 6″ in diameter) spectrum from the contaminating sources within Circinus that fall into the *NuSTAR* PSF. These contaminating sources were modeled individually and their spectra extrapolated into the *NuSTAR* band. Both the nuclear emission and the contamination have strong signatures of cold reflection off dense material, with high EW fluorescent Fe lines and hard continua indicative of a Compton hump. We combined the different instruments to produce a broadband spectrum and modeled it with a combination of the nuclear and contamination models. The Compton-scattered components were modeled using the `pexmon`, `MYTorus` and `Torus` models.

Compton scattering modeled with `pexmon` on its own was unable to reproduce the curvature of the high-energy spectra, in particular the hump at around 30 keV. This model assumes the reflecting material is a slab of infinite optical depth, which places the Compton hump at around 20 keV. In order to shift the hump to higher energies and produce additional curvature, it either requires super-solar abundances or a low-energy cut-off

in the incident power law. This model is useful for applications requiring accretion disk reflection, where the column density is expected to be of the order of $\sim 10^{31}$ cm^{-2} (Svensson & Zdziarski 1994) and a slab geometry is expected. However, its applicability is limited for other scattering media, such as the torus or galactic scale reflection nebulae, which can have significantly lower column densities and different geometries.. The only configuration where pexmon produced a good fit included a cut-off in the original power law at the relatively low energy of 28 keV and a transmitted power-law component of much higher normalization that dominates the total spectrum above 30 keV. This model was subsequently ruled out by the lack of variability seen in the 30–79 keV band, which, according to this spectral decomposition, should correspond to the transmitted component.

Previous fits to the X-ray spectrum of Circinus using the pexrav model for the Compton-scattered component produced flat incident power law slopes ($\Gamma \sim 1.3$–1.7) and low cut-off energies of about 50–80 keV (Matt et al. 1999; Dadina 2007), similar to our results using pexmon. The highest-energy *NuSTAR* and *Swift* BAT spectra, however, are underpredicted by these models, mainly due to the low energy of the power law cut-off.

The models Torus and MYTorus produce Compton-scattered and transmitted components self consistently through a dense material of finite and variable column density. Both models have axisymmetric geometries, a sphere with polar conical holes in the first case and a torus in the second. We tested different configurations, considering smooth and patchy implementations of the MYTorus model for the nuclear and contamination components, as well as a spherical torus modeled with Torus for the nucleus plus MYTorus or pexmon components for the contamination. In all the MYTorus configurations, a cut-off/termination energy in the intrinsic AGN continuum at about 160 keV improved the fit. Torus does not incorporate cut-off energy as a model parameter, but this model produced a better fit than the default configuration MYTorus model with no cut-off. Therefore, it is possible that Torus would produce the best fit if a cut-off energy were implemented in this model. Given this limitation, it is not possible to prefer one geometry over the other.

Below we summarize the common features of the best-fitting models for all the torus geometries tested. Both models reproduce the spectrum of Circinus accurately without resorting to super-solar metallicities. A cut-off in the AGN intrinsic power-law spectrum was preferred by all the different configurations tested; this cut-off/termination was found to be between 100 and 200 keV with a best fit at 160 keV, instead of the 28 keV of the pexmon fit. We stress again that the MYTorus termination energy is not equivalent to a rollover in the intrinsic power law, which is usually referred to as a cut-off, but rather to an abrupt decrease in intrinsic flux. Therefore, these energies should not be interpreted as cut-off energies in the usual sense. The nuclear column densities are in the range $N_{\rm H} = (6.6$–$10) \times 10^{24}$ cm^{-2} and photon indices of the incident AGN spectrum in the range $\Gamma = 2.2$–2.4, much steeper than in the pexmon fits. The differences in $N_{\rm H}$ and Γ values between models are significantly larger than the statistical errors, as can be seen in Table 3, and thus are only meaningful when considering a particular geometric model.

The high line-of-sight column density only allows a very small fraction of the intrinsic AGN continuum to shine through, even at the highest energies probed. In the best-fitting models, the transmitted component only accounts for 7% of the 30–80 keV flux. The variability of the high-energy (30–79 keV) emission is consistent with counting noise only so no intrinsic variability is detected in this band. By comparing the amplitude and timescales of the variability of similar but unobscured sources, we conclude that the high-energy emission corresponds to Compton-scattered rather than transmitted power-law continuum, in agreement with the favored spectral models.

In unobscured sources, where the power-law slope can be measured with less uncertainty, a slope of $\Gamma = 2.3$ is not unusual, although it is toward the high end of the distribution of measured slopes. The correlation found between Γ and accretion rate, however, does point to steeper slopes at higher accretion rates. For the values from the literature quoted in Section 1, the accretion rate in terms of Eddington luminosity in Circinus is $L/L_{\rm Edd} = 0.2$. According to Shemmer et al. (2006), the corresponding power-law slope is about $\Gamma = 2.1$, and Fanali et al. (2013) predicts it to be $\Gamma = 2.4 \pm 0.1$, straddling our measured values of $\Gamma = 2.2$–2.4.

The unobscured 2–10 keV power law flux in the default configuration of MYTorus with termination energies of 500, 160, and 100 keV (models 6, 7, 8, respectively) as well as in the Torus model fit (model 11) is in the range $(1.1$–$2.4) \times 10^{-9}$ erg s^{-1} cm^{-2}. The decoupled MYTorus models with power law cut-off/termination energies of 500 and 160 keV, where the normalizations of the Compton scattered and transmitted components vary freely (models 9 and 10) resulted in vanishing transmitted components such that an intrinsic flux could not be estimated for them. This range of fluxes corresponds to an isotropic 2–10 keV luminosity of $(2.3$–$5.1) \times 10^{42}$ erg s^{-1}. This equals 6%–13% of the bolometric luminosity estimated by Moorwood et al. (1996) from mid-IR spectroscopy, where most of the nuclear mid-IR flux is identified with reprocessed AGN emission. This $L_{2-10}/L_{\rm bol}$ ratio is within the range of X-ray to bolometric luminosity ratios found in type 1 AGN (e.g., Elvis et al. 1986; Fanali et al. 2013).

Gandhi et al. (2009) calculate the $L_{2-10\,{\rm keV}}/L_{12\,\mu{\rm m}}$ using nuclear IR luminosities, as opposed to the large aperture ISO values quoted above, finding an almost linear relation with 0 intercept. Asmus et al. (2014) measured a nuclear 12 μm IR flux for Circinus of 8.3 ± 1.0 Jy, using ground based high angular resolution imaging. This nuclear IR value corresponds to a $L_{12\,\mu{\rm m}} = 4.3 \times 10^{42}$ erg s^{-1} which is within the range of unobscured $L_{2-10\,{\rm keV}}$ luminosities quoted above, precisely as predicted by the relation of Gandhi et al. (2009). The transmitted component in the best-fitting pexmon model, on the other hand, has a 2–10 keV flux of 4.0×10^{-8} erg s^{-1} cm^{-2}, corresponding to an unobscured luminosity of $L_{2-10\,{\rm keV}} = 8.4 \times 10^{43}$ erg s^{-1}, 36 times larger than that expected from the 12 μm flux. The fact that the interpretation of the high-energy X-ray spectrum as transmitted rather than Compton scattered emission results in a *larger* intrinsic X-ray flux might seem counter intuitive. At these high column densities, however, the suppression of the transmitted power law by Compton scattering is very significant, so that the Compton-scattered component dominates over the transmitted component when they are modeled self consistently. For the transmitted power law to reach the observed 30–80 keV fluxes, its intrinsic luminosity needs to be about 40 times larger than that of the power law required to produce the same flux level as a Compton-scattered component.

The total—nuclear plus contamination—Compton-scattered fractions are 0.43%–0.65% of the intrinsic AGN continuum in the 2–10 keV band and 5.8%–7.7% in the 2–100 keV band for the MYTorus models and 1.1% and 12% in the same

energy ranges for the best-fitting Torus model. Note that in the last model the Compton-scattered component incorporates the transmitted flux, so these ratios are slightly overestimated.

The galactic Compton scattering probably represents AGN continuum emission scattered by dense clouds in different locations of the galaxy. In the best-fitting model, the average spectrum of these distant scatterers corresponds to clouds of $N_{\rm H} = 3.9$–7.4×10^{24} cm^{-2}. These values are similar to but in most cases lower than those found for the nuclear Compton scatterer (i.e., the torus) of $N_{\rm H} = 6.6$–10×10^{24} cm^{-2}. The galactic Compton scattering spectrum is therefore harder than the nuclear component, as can be seen in the dotted red lines in Figure 14. Similar large-scale reflection nebulae have been observed in the Galactic center, where strong Fe fluorescent emission tracks the position of known molecular clouds (Sunyaev et al. 1993; Koyama et al. 1996; Murakami et al. 2001). These lines together with their hard X-ray continua (Revnivtsev et al. 2004) are interpreted as a reflection of past AGN activity in Sgr A*. Modeling the X-ray spectrum of these reflection nebulae, Ponti et al. (2010) find column densities of up to 8×10^{23} cm^{-2}, somewhat lower than our findings in Circinus. Given the large gas content of Circinus compared to our Galactic center, we can probably expect a larger covering fraction and column densities in the former. We also note that since the strength of the galactic Compton scattering component should scale with the intrinsic AGN power, a similar contamination is likely also important in higher luminosity sources. For lower spatial resolution observatories as well as for more distant AGN, contamination of the nuclear spectrum can be significant.

The Compton-scattered component in the Circinus galaxy appears in all directions, not only toward the ionization cone, which should have a clear view of the nucleus. The lack of "shadow" regions in the diffuse gas reflection argues for a patchy or leaky torus, which allows the AGN continuum to illuminate material in all directions. This type of clumpy torus model is also favored by the shape of the IR spectra of both type 1 and type 2 AGN (Elitzur & Shlosman 2006). The nuclear distribution of the Compton-scattered light from Circinus within a few arcsec from the center was recently studied by Marinucci et al. (2013), who inferred a clumpy Compton-thick scatterer about 100 pc across. The implications for the shape of this Compton scattering material from large-scale reflection features will be studied further in a separate paper (F. E. Bauer et al., in preparation).

Finally, we studied the long-term variability of sources in the Circinus region. The nuclear spectra, extracted from *XMM-Newton* pn data within 11″ of the center, are remarkably constant over the 12 yr that separate the *XMM-Newton* exposures and is consistent with no evolution of the flux or spectrum. The other two brightest point sources show strong evolution: the XRB CGX1 drops its average flux by a factor of 2.3 and the SN CGX2 evolving to lower temperatures. Observations made with resolutions worse then ∼5′, will also be contaminated by the bright ULX5 up to energies over 30 keV (Walton et al. 2013). Such variable sources must be taken into account to correctly interpret the spectra of different epochs.

We thank the anonymous referee for a thorough review and many useful suggestions that improved this paper. This work was supported under NASA Contract No. NNG08FD60C, and made use of data from the *NuSTAR* mission, a project led by the California Institute of Technology, managed by the Jet Propulsion Laboratory, and funded by the National Aeronautics and Space Administration. We thank the *NuSTAR* Operations, Software, and Calibration teams for support with the execution and analysis of these observations. This research has made use of the *NuSTAR* Data Analysis Software (NuSTARDAS) jointly developed by the ASI Science Data Center (ASDC, Italy) and the California Institute of Technology (USA). We acknowledge financial support from Basal-CATA PFB-06/2007 (FEB), CONICYT-Chile FONDECYT 1140304 (PA), 1141218 (FEB), 1120061 (ET), and Anillo ACT1101 (PA, FEB, ET). A.C., A.M., and G.M. acknowledge the ASI-INAF grant I/037/12/0. W.N.B. and B.L. acknowledge support from Caltech NuSTAR subcontract 44A-1092750 and NASA ADP grant NNX10AC99G. M.K. gratefully acknowledges support from Swiss National Science Foundation Grant PP00P2_138979/1. P.G. thanks STFC for support (grant reference ST/J003697/1).

REFERENCES

Arévalo, P., Churazov, E., Zhuravleva, I., Hernández-Monteagudo, C., & Revnivtsev, M. 2012, MNRAS, 426, 1793
Asmus, D., Hönig, S. F., Gandhi, P., Smette, A., & Duschl, W. J. 2014, MNRAS, 439, 1648
Bauer, F. E., Brandt, W. N., Sambruna, R. M., et al. 2001, AJ, 122, 182
Baumgartner, W. H., Tueller, J., Markwardt, C. B., et al. 2013, ApJS, 207, 19
Bianchi, S., Matt, G., Fiore, F., et al. 2002, A&A, 396, 793
Bianchi, S., Matt, G., & Iwasawa, K. 2001, MNRAS, 322, 669
Boldt, E. 1987, PhR, 146, 215
Brightman, M., & Nandra, K. 2011, MNRAS, 413, 1206
Brinkmann, W., Siebert, J., & Boller, T. 1994, A&A, 281, 355
Broos, P. S., Townsley, L. K., Feigelson, E. D., et al. 2010, ApJ, 714, 1582
Dadina, M. 2007, A&A, 461, 1209
Elitzur, M., & Shlosman, I. 2006, ApJL, 648, L101
Elmouttie, M., Haynes, R. F., Jones, K. L., Sadler, E. M., & Ehle, M. 1998, MNRAS, 297, 1202
Elvis, M., Green, R. F., Bechtold, J., et al. 1986, ApJ, 310, 291
Fanali, R., Caccianiga, A., Severgnini, P., et al. 2013, MNRAS, 433, 648
Freeman, K. C., Karlsson, B., Lynga, G., et al. 1977, A&A, 55, 445
Frontera, F., Costa, E., dal Fiume, D., et al. 1997, A&AS, 122, 357
Gandhi, P., Horst, H., Smette, A., et al. 2009, A&A, 502, 457
Gehrels, N., Chincarini, G., Giommi, P., & Mason, K. O. 2004, ApJ, 611, 1005
Grandi, P., Guainazzi, M., Mineo, T., et al. 1997, A&A, 325, L17
Greenhill, L. J., Booth, R. S., Ellingsen, S. P., et al. 2003, ApJ, 590, 162
Grimm, H.-J., Gilfanov, M., & Sunyaev, R. 2003, MNRAS, 339, 793
Guainazzi, M., & Bianchi, S. 2007, MNRAS, 374, 1290
Guainazzi, M., Matt, G., Antonelli, L. A., et al. 1999, MNRAS, 310, 10
Harrison, F. A., Craig, W. W., Christensen, F. E., et al. 2013, ApJ, 770, 103
Iwasawa, K., Koyama, K., Awaki, H., et al. 1993, ApJ, 409, 155
Koyama, K., Maeda, Y., Sonobe, T., et al. 1996, PASJ, 48, 249
Lehmer, B. D., Alexander, D. M., Bauer, F. E., et al. 2010, ApJ, 724, 559
Magdziarz, P., & Zdziarski, A. A. 1995, MNRAS, 273, 837
Maiolino, R., Krabbe, A., Thatte, N., & Genzel, R. 1998, ApJ, 493, 650
Marconi, A., Moorwood, A. F. M., Origlia, L., & Oliva, E. 1994, Msngr, 78, 20
Marinucci, A., Miniutti, G., Bianchi, S., Matt, G., & Risaliti, G. 2013, MNRAS, 436, 2500
Markowitz, A., Edelson, R., Vaughan, S., et al. 2003, ApJ, 593, 96
Markowitz, A., Papadakis, I., Arévalo, P., et al. 2007, ApJ, 656, 116
Massaro, F., Bianchi, S., Matt, G., D'Onofrio, E., & Nicastro, F. 2006, A&A, 455, 153
Matt, G., Fiore, F., Perola, G. C., et al. 1996, MNRAS, 281, L69
Matt, G., Guainazzi, M., Maiolino, R., et al. 1999, A&A, 341, L39
McClintock, J. E., & Remillard, R. A. 2006, in Black Hole Binaries, ed. W. H. G. Lewin & M. van der Klis (Cambridge: Cambridge Univ. Press), 157
McHardy, I. M., Gunn, K. F., Uttley, P., & Goad, M. R. 2005, MNRAS, 359, 1469
McHardy, I. M., Koerding, E., Knigge, C., Uttley, P., & Fender, R. P. 2006, Natur, 444, 730
McHardy, I. M., Papadakis, I. E., Uttley, P., Page, M. J., & Mason, K. O. 2004, MNRAS, 348, 783
Mingo, B., Hardcastle, M. J., Croston, J. H., et al. 2012, ApJ, 758, 95
Mitsuda, K., Bautz, M., Inoue, H., & Kelley, R. L. 2007, PASJ, 59, 1
Molendi, S., Bianchi, S., & Matt, G. 2003, MNRAS, 343, L1

Moorwood, A. F. M., & Glass, I. S. 1984, A&A, 135, 281
Moorwood, A. F. M., Lutz, D., Oliva, E., et al. 1996, A&A, 315, L109
Murakami, H., Koyama, K., Tsujimoto, M., Maeda, Y., & Sakano, M. 2001, ApJ, 550, 297
Nevalainen, J., David, L., & Guainazzi, M. 2010, A&A, 523, A22
Oliva, E., Marconi, A., Cimatti, A., & Alighieri, S. D. S. 1998, A&A, 329, L21
Oliva, E., Salvati, M., Moorwood, A. F. M., & Marconi, A. 1994, A&A, 288, 457
Peterson, B. M., Ferrarese, L., Gilbert, K. M., et al. 2004, ApJ, 613, 682
Ponti, G., Terrier, R., Goldwurm, A., Belanger, G., & Trap, G. 2010, ApJ, 714, 732
Puccetti, S., Comastri, A., Fiore, F., et al. 2014, ApJ, submitted
Revnivtsev, M. G., Churazov, E. M., Sazonov, S. Y., et al. 2004, A&A, 425, L49
Roy, A. L., Goss, W. M., & Anantharamaiah, K. R. 2008, A&A, 483, 79
Sambruna, R. M., Netzer, H., Kaspi, S., et al. 2001, ApJL, 546, L13
Shemmer, O., Brandt, W. N., Netzer, H., Maiolino, R., & Kaspi, S. 2006, ApJL, 646, L29
Shu, X. W., Yaqoob, T., & Wang, J. X. 2011, ApJ, 738, 147
Sikora, M., Stawarz, Ł., & Lasota, J.-P. 2007, ApJ, 658, 815
Smith, D. A., & Wilson, A. S. 2001, ApJ, 557, 180
Sunyaev, R. A., Markevitch, M., & Pavlinsky, M. 1993, ApJ, 407, 606
Svensson, R., & Zdziarski, A. A. 1994, ApJ, 436, 599
Walton, D. J., Fuerst, F., Harrison, F. A., et al. 2013, ApJ, 779, 148
Wik, D. R., Hornstrup, A., Molendi, S., et al. 2014, arXiv:1403.2722
Woo, J.-H., & Urry, C. M. 2002, ApJ, 579, 530
Yang, Y., Wilson, A. S., Matt, G., Terashima, Y., & Greenhill, L. J. 2009, ApJ, 691, 131
Yaqoob, T. 2012, MNRAS, 423, 3360